BILINGUAL PUBLISHING GROUP

Journal of Atmospheric Science Research

https://journals.bilpubgroup.com/index.php/jasr

ARTICLE

The Hydrospheric Solar Correlation Dipole: Mapping, Interpretations, and Forecasting

Michael Gary Wallace [1*], ***Yifeng Wang*** [2], ***Boris Faybishenko*** [3]

[1] *Abeqas Hydrosciences LLC, Albuquerque, NM 87110, USA*

[2] *Sandia National Laboratories, Albuquerque, NM 87185, USA; ywang@sandia.gov*

[3] *Lawrence Berkeley National Laboratory, Berkeley, CA 94720, USA; bafaybishenko@lbl.gov*

ABSTRACT

A meridional dipole, centered near 180° E, characterizes solar correlations to oceanic and atmospheric parameters—salinity, ocean vertical velocities, temperatures, atmospheric moisture, winds, cloud cover, geopotential heights, carbon dioxide (CO_2) fluxes, and ozone (O_3)—over several years of lag, with opposing correlation signs on either side of the dipole axis. Ocean correlations are stronger and more persistent than atmospheric ones; most fields intensify equatorward through the third lag-year before decaying over subsequent years. We propose, as a hypothesis for future testing, that this pattern traces global energy transport along an expanded Hadley Cell framework, with opposing correlation zones arising from latent heat exchange at the ocean surface and tropopause. Statistical significance is assessed using methods that account for serial autocorrelation (AC) and correct for multiple comparisons across variables and lags. Where correlations are highest, we propose solar activity as a useful baseline hypothesis for evaluating regional climate trends—an improvement, in these specific regions, over the null hypothesis of random states; we do not extend this claim more broadly. We further examine predictive value: reviewing an earlier cross-regression-moving-average (CRMA) case study and presenting a new forecast of five-year trailing rainfall at an Upper Colorado Basin (US) site, three years ahead. Hindcast results show the solar-regressed exercise is more skillful than the standard auto-regression-moving-average (ARMA) techniques, suggesting value in anticipating climate extremes (drought vs. fluvial) in high-correlation regions.

*CORRESPONDING AUTHOR:
Michael Gary Wallace, Abeqas Hydrosciences LLC, Albuquerque, NM 87110, USA; Email: mwa@abeqas.com

ARTICLE INFO
Received: 4 March 2026 | Revised: 27 May 2026 | Accepted: 8 June 2026 | Published Online: 16 June 2026
DOI: https://doi.org/10.30564/jasr.v9i3.13249

CITATION
Wallace, M.G., Wang, Y., Faybishenko, B., 2026. The Hydrospheric Solar Correlation Dipole: Mapping, Interpretations, and Forecasting. Journal of Atmospheric Science Research. 9(3): 20–67. DOI: https://doi.org/10.30564/jasr.v9i3.13249

Keywords: Solar Activity; Divergence of Latent Heat; Climate Forecasting; Atmospheric and Ocean Circulation; Hydrosphere

1. Introduction

The coupled moist atmosphere-ocean continuum, collectively known as the hydrosphere, is widely understood to be significantly driven by solar radiation, yet studies in all related forms, from observation to time series analyses and on to numerical modeling have not extensively documented this or widely applied it to climate forecasting at any scale. Moreover, modern and influential studies such as Gray et al. [1] subordinate solar climate forcing to the bottom of a long list of potential climate drivers. Most notably, the Gray et al. hierarchy of solar forcing is embodied in the scientific basis papers of the UN IPCC (United Nations Intergovernmental Panel on Climate Change), notably in Chapter 8 by Myhre et al. in 2013 [2]. This reference is used interchangeably with the acronym WG1AR5, which stands for "The Working Group I contributions to the Fifth Assessment Report". Along with Chapter 7 of the subsequent WG1AR6 report [3], certainty of the primacy of anthropogenic greenhouse gases (primarily CO_2) in the hierarchy of climate causation is emphasized.

The hierarchy is consistent between the studies and is clearly illustrated by Figure 8.15 in the Intergovernmental Panel on Climate Change (IPCC) [2]. In the WG1AR5 figure, the solar component of the forcing hierarchy is indicated by the thinnest bar and placed at the bottom of the chart. Those documents and the Gray et al. study are cited by many papers ranging from paleoclimate interpretations such as van Dijk et al. [4], to contemporary climate attribution studies including Smith et al. [5] which principally attribute decadal climate forcing to greenhouse gases. Notably, the Myhre et al. authors close their conclusions with the following statement on p. 661: "increasing levels of evidence and degrees of agreement are correlated with increasing confidence."

Models are typically termed either Earth Systems Models (ESMs) or Global Circulation Models (GCMs, gcms). Each is used interchangeably in this study. It is clear that ESM-based studies have been extensively used in both WG1AR reports. The citations include ESM-aligned papers that explore the attribution/causality of intermittent extreme climate events including work by Otto [6], Perkins-Kirkpatrick et al. [7], Risser et al. [8] and Hammerling et al. [9]. Solar activity is not a driver of primary application in these publications.

A related consideration applies for contemporary "detection" studies of climate trends. Most of those trend studies lack attention to lagged solar or any other external correlations. Instead, attributions to causes for any trends are developed specifically through models, and often in that case to ESMs [10,11]. Both single out trend analysis as a detection exercise, followed by an attribution section which exclusively relies upon ESMs. As subsequently described, ESMs do not incorporate solar dynamics. Accordingly, solar forcing components are excluded from both the detection and the attribution components in these studies. Moreover, the studies use models as surrogates for natural variability. This appears to defeat the purpose of the null-hypothesis, as explored in the Discussion section. Finally, in contrast to the current study, the detection studies don't widely appear to include testable forecasts. This challenges any robust skill-based ranking of their performance, whether through hindcasts or forecasts.

The missing attention to solar activity in trend detection and simulation-based attribution work is of added interest because a solar-based climate forecast [12] has already demonstrated quantitative skill at anticipating forecast extreme climate events (drought versus pluvial) better than the widely used autoregressive integrated moving average (ARIMA) and/or ARMA methodologies. In achieving that distinction, the Wallace study poses a challenge to the interpretations and conclusions in "detection and attribution" (D&A) products.

Computational modeling exercises have long offered important benefits but only when skill can at least be demonstrated, as a minimum requirement. One obstacle to better physical emulation skill includes the use of parameterizations. Parameterizations, or lookup tables, define away any dynamic interaction, often defeating the purpose of the model. It would not be surprising if such parameterized models expressed poor predictive skill. In fact, the wide adoption of ESMs to the Gray et al. [1] and Myhre et al. [2] hierarchies has not led to a skillful track record in annual- to decadal-scaled predictions of important parameters. Those parameters range from surface hydrology to atmospheric rainfall and temperature and extend to ocean temperature and salinity in any given region.

For example, some recent papers including Bracco et al.[13] and Balaji et al.[14] have explored patterns of model skill in the climate field. The recent climate model review paper by Bracco et al. described attempts to improve accuracy. Although this paper claimed that Machine Learning (ML) has improved climate predictability, it relied primarily on an ENSO (El Niño Southern Oscillation) example from 2019 which compared only hindcasts[15]. However, all researchers accept that hindcasts alone are not sufficient for evaluations of the potential forecast fidelity of any model, especially when the hindcasts are not skillful. In addition to the Bracco et al. study, a growing number of related examples chronicle the less than modest skill worldwide. For example, the work by Kroll et al.[16], indicates the shortcomings of climate models to capture the essential features of the Intertropical Convergence Zone (ITCZ). Also, a recent report of climate model departures from observations of "Mediterranean drying" is featured by Seager et al.[17].

Numerous other examples can be found of this skill challenge, and at least some bypass discussion of solar causality, even as their ubiquity in peer review might imply compounding evidence of greenhouse gas climate causality. In comparison, a verified and skillful solar-based forecast might add significant weight to any re-emerging solar causality claim. As solar causality-grounded forecasts rise to the skill challenge, a small but growing number of models are already incorporating solar dynamics more explicitly. In each and any case, the parameterizations of the deterministic and statistical models are critical to the acceptance and validity of both hindcasts and forecasts. This paper includes a parallel focus on more statistically aligned and we argue, more physically-based, solar predictive potential. Finally, we introduce a simple skill evaluation method for almost any specific forecast and apply it to ours.

2. Data and Methods

This study targets the development of a set of maps and practical interpretations of the statistically significant lagged correlations, both positive and negative, to solar activity, for water-related variables. **Table A1** provides a convenient p-value guide used in interpretation of the contours for each featured correlation map and profile, depending upon the source data, the number of continuous annual entries and the resulting linear correlation. The correlation plots are always dimensionless by convention.

For multi-year hydroclimate diagnostics and projections to provide significant value, it is essential to operate within a conceptual model that aligns with all relevant observational data, including annual to decadal-scale solar activity. Additionally, as in Wallace's[12] study, it remains advantageous to use climatologically scaled geospatial reanalysis datasets which offer consistent, continuous, and comprehensive coverage of key parameters worldwide.

Consequently, as detailed throughout **Appendix A**, including **Tables A2** (data references) and **A3** (spatial and temporal scales of each data set), this study primarily relies on three datasets from ECMWF (European Center for Medium-Range Weather Forecasts). Also, two ocean-based datasets are utilized: NASA's Estimating the Circulation and Climate of the Ocean (ECCO) and products associated with Southern Ocean Carbon and Climate Observations and Modeling (SOCCOM)[18–21].

Beyond those exercises and resources, this study considers the potential root causes of the unique meridional dipole correlation trends subsequently identified in the Results section. In particular, latent heat divergence phenomena are mapped and compared to other assets to develop interpretations featured in the Discussion section. Finally, a linear regression forecast exercise is conducted for one of the same general locations used in the earlier Wallace study. This exercise includes a hindcast and a projection. The projection is intended to be evaluated after the three subsequent years of observations have caught up. The hindcast is examined with respect to skill and to disambiguate from natural persistency effects. This is achieved through the common technique of calculating the autocorrelation of the residual series, which we term ACOR for brevity.

A variety of additional methods and resources are pointed to and/or discussed in this document but many are described only for context and/or comparison. The final methods applied were the Granger causality test documented in **Figure A9** and the Nash-Sutcliffe Efficiency metric (NSE) documented in **Table A4**, for two independent evaluations of the skill of the hindcast in the above exercise.

3. Results

3.1. Models and Gaps of Solar Forcing through Latent Heat Dynamics

As noted, climate models and related products have developed a radiant forcing approach to the anticipation of global climate change. Within that framework, Gregory and Forster [22] introduced the concept of Transient Climate Response (TCR), and indicated a linear relation between CO_2 concentration and global average surface temperature. Citing simulations and observations, the study concluded that global temperatures would increase ~1.8° (K or C) upon a 100% increase in CO_2. The authors framed this somewhat differently with an assumption that this would take 100 years, given a 1% increase in global CO_2 concentration per year. But the ultimate question of how much, and in what direction globally-averaged surface temperature will shift, due to a 1% increase in CO_2, or any other forcing factor, has been an important consideration for many researchers and others in policy who consult Myhre et al. [2].

It is initially convenient to compare this climate sensitivity against a solar forcing estimate which premiered in 1974 by Paltridge [23]. The Paltridge study also addressed global energy balance data and interpretations, including consideration of global cloud cover and latent heat. Paltridge developed linear forcing estimates for solar activity upon both moisture content Θ and surface temperature T. That analysis considered the change in the "solar constant" of 6.6% over any year, simply based upon the change in the distance from the Earth to the sun between July 4 (aphelion) and January 3 (perihelion). The global temperature forcing estimate of ~0.35° (K or C) upon a 1% change in the "solar constant" is much larger in a relative sense, compared to the Gregory and Forster estimate for CO_2 sensitivity.

This divergence in calculated sensitivities between global CO_2 forcing and global solar forcing is not widely recognized, and neither sensitivity value has been authenticated. But we feel it serves an initial purpose to highlight the different approaches, specifically to global climate sensitivity that exist in the literature. Moreover, this highlights a much different focus in those studies, than our method of mapping solar activity multi-year correlations with synoptic and other scales of climate. In any case, the WG1AR5 and WG1AR6 frameworks, which both exclude solar forcing dominance, have long persisted as the principal vehicle for climate modeling on both global and smaller scales, from synoptic to local.

Earlier, we noted the association of WG1AR5 and WG1AR6 products with a number of examples which did not demonstrate robust predictive skill. We feel that even one example is important towards continuous process improvement and would justify subsequent papers in its own right. In any case, the persistent shortcomings in skill throughout the global circulation modeling (GCM) publications have recently come to a head as summarized by Balaji et al. [14]. That paper explores many of the challenges to better prognostic skill, and their interpretation of the reasons for these deficiencies. In breaking those out, the paper summarizes the causal factors that are intended to be simulated and accounted for through the discretized partial differential equation given by:

$$\frac{\partial x}{\partial t} = R(x) + U(x) + P(x) + F \tag{1}$$

Where x is a state vector of the circulating atmospheric or ocean variable under consideration, t is time, and R(x) + U(x) represent the full Navier-Stokes formulation for the circulating species. Notably, R represents the "resolved" features, i.e., the features that can be directly simulated without reliance upon look-up tables, and U represents the "unresolved" features. Those are the features for which extensive parameterizations (look-up tables) have been tried. The number of parameterizations is sizable as the paper documents. Most specific to our investigation are the final equation elements P(x) + F. P represents other thermodynamic contributions related to moist adiabatics, including by this definition, latent heat. As the key state-changing climate variable, moisture's latent heat is also a primary foundation of our interest in featured solar correlations. In that respect, the final F component of Equation (1) relates to exogenous factors, and the authors include solar radiation in that category along with numerous other candidates, which follows the same general hierarchy as Gray et al. [1].

The substance of the Balaji and other papers suggests the significant scope of the parameterizations that pose a challenge to many of the original purposes of dynamic climate analysis. GCMs often deploy simple look-up tables limited to solar maxima and minima. Notably, those parameterized inputs do not include any dynamics that stem from sunspot number or total solar irradiance time series. Accordingly, the impact of solar activity upon any simulated variable cannot be authenticated in most GCMs, even if its forcing magnitude were increased several-fold. In comparison as detailed in this study, we first focused on capturing the dynamics of solar activity through direct sunspot number time series (SSNs).

We also regard latent heat and its magnitude and sign changes associated with the state changes of water as an essential record of solar activity's impact upon the hydrosphere. In comparison, for most GCMs, latent heat is only indirectly accounted for. In that regard, it appears to be largely an input to the climate modeling systems that align to WG1AR5, and not an output. The primary purpose of latent heat in those GCMs appears to be limited to parameterization of gravity wave impacts on circulation [24,25].

Some responsive work has recently emerged. One strategy has been to develop better parameterizations, such as Wang et al. [26], which use machine learning in conjunction with explicit state simulations of convection factors including moist adiabatics and solar forcing. These parameterizations were shown to have significant skill in some respects. However, they are currently self-identified as preliminary studies. The more explicit simulations of this strategy, along with related previous attention profiled by Mantsis et al. [27], might gain further traction as working GCMs if improvements in model resolution and performance time continue to develop.

In spite of growing awareness, the multi-year advance prediction skills of models are not measured by the major simulation benchmarking exercises such as the Climate Model Intercomparison Projects (CMIP, see Taylor et al. [28] or Smith et al. [29] for a later intercomparison). Those projects have focused on the comparison of models to each other, and not to observations. Additionally, studies such as the Smith et al. paper tout "robust skill" in the title, but instead feature the periodic resetting of model results (reinitialization) to better match observations. The prevalence of reinitialization practices and the omission of raw skill investigation in such benchmarks highlights the challenges for more skillful alternatives.

3.2. Emergence of Solar Correlation Evidence

Regardless of the magnitude of climate attribution work, the extents, mechanisms, and positive and negative signatures of solar radiative forcing, from the bottom of the ocean to the top of the hydrosphere remain poorly known. However, through a methodical set of exercises based on reanalysis data, a more explicit tracing of solar energy is beginning to emerge across annual-to-decadal scales for any given atmospheric or oceanic circuit. Our tracing of this solar-attributed energy is again informed by changes in divergence of latent heat, a critical aspect of water's state changes.

Should correlations between solar activity and atmospheric variables turn out to be statistically significant, then in addition to this evidence of a degree of causality, empirical projections and linear regression solutions might apply to predict some atmospheric and oceanic patterns with greater fidelity and over longer timescales than ever. Our analysis suggests that multi-annual lagged correlation signatures of solar activity to many components of satellite reanalysis data constitute the basis for that tracing.

The significance of linear forcing of the atmospheric moist Hadley Cell (HC) by solar activity over multiple years was explored by a number of papers including Labitzke and Van Loon in 1997 [30], which consolidated a number of their related studies for the preceding decade, and Meehl and Arblaster in 2009 [31] which also cited works by Labitzke and Van Loon [30]. The subsequent paper by Wallace [12] applied regression mapping of geostrophic reanalyses and individual river station data from high-altitude, mid-latitude hydrologic catchments. Those included the Andes, the Himalayas, and the Rocky Mountains. Wallace's interpretations about solar forcing of climate were significantly different from the work by Gray et. al. [1], which did not explicitly consider the HC or latent heat. Citing others, the Wallace paper identified the Western Equatorial Pacific (WEP) as the primary source of Hadley-driven moisture transport to middle latitudes. Furthermore, the Wallace paper identified strong lagged linear correlations between variables ranging from trade winds, divergence of latent energy (LEDIV), and outgoing longwave radiation (OLR) to decadal-scale solar activity.

Overlapping studies of the same topic of solar correlations to WEP conditions were published in 2016 by Xiao et al. [32] and in 2023 by Huo et al. [33]. The Xiao et al. paper noted a dipole in the correlation between solar activity and OLR, but did not explicitly connect that to latent heat, although it did refer to other aspects of convection. Notably the paper filtered out the ENSO signal from the correlation results but still found significant solar correlations, again at an equivalent lag of two years and in a dipole pattern (positive and negative paired contours), which the authors additionally connected to circulation over the WEP. The subsequent paper by Huo et al.[33] identified a dipole in ocean heat content across the Eastern Tropical Pacific with statistically significant lagged solar correlations. That paper explored the impacts of solar dynamics upon ocean heat content for the same synoptic region as the Xiao et al.[32] paper, focusing again on a 2-year lag and using models (with parameterizations) to explore the variability space.

Wallace[12] noted other connections associated with the WEP and a strong correlation of the (nearby) western ENSO boundary to solar activity. The study featured the use of that in a forecasting exercise but otherwise did not explore the dipole that these earlier researchers identified. The Wallace paper categorized those energy parameters along with several other variables, including Evaporation minus Precipitation (EP) and geopotential height (Z), as consequential to the limbs of the hydrologic cycle that impacted rainfall and streamflows across the Western US, among other locations. In addition, the paper developed projections based on the conceptual model for solar driving of the full Hadley circulation. The largely moist Hadley circulation extends from the equator to all middle latitudes and throughout the troposphere. Although much about the Hadley circulation along with the related Brewer-Dobson and Walker circulations are roughly understood, and although earlier studies speculated on a solar driver of these circulations, contemporary citations for causal mechanisms now routinely lack solar attributions[34,35].

The Wallace paper developed statistically significant, multi-year lagged correlations between streamflow time series and solar activity and applied them in prediction exercises. This was based on a stepwise conceptualization that an increase in solar activity diminishes meridional equatorial trade winds (TWWP), notably along the Western Equatorial Pacific, and that this change leads to a shift in Hadley-related moisture circulation across distant high-altitude, mid-latitude hydrologic catchments, such as the Southern Rocky Mountains.

The paper notably demonstrated an improvement over natural variability (the de facto null hypothesis for all climate interpretations) by featuring comparisons of solar-based correlations to autocorrelation series for each stream. This demonstration was supported by numerous goodness-of-fit approaches, including Pearson Correlation, RMSE, Chi-Squared (χ^2) and Kolmogorov-Smirnov tests. The regressions were additionally compared to autocorrelation. The solar regression metrics typically scored higher, and a forecast of Animas River and other flows was included in the publication for subsequent transparent falsification.

The Animas River expressed the highest lagged correlations directly to solar activity and so a projection of its five-year trailing average (5yta) flows for three years in advance (years 2017, 2018 and 2019) was included. Another forecast exercise sought to project the Animas annual flow for 2 years in advance. The 5yta Animas 3-year projection exercise is recaptured in **Figure 1a**. Because the exercise was submitted with the paper in late 2016 and because the paper was not published until early 2019, the chart has been updated to reflect the subsequent observations (red solid line), allowing for a fuller diagnostic of the exercise. Our diagnostic is featured in **Figure 1b**, as comparisons of the forecast (and hindcast) errors versus the magnitude of the discharges. Notably the cross-regression forecast (TWWP) showed greater overall accuracy than the autoregression forecast. Moreover, the TWWP forecast was more skillful at representing the ‘extremes’ of the Animas flows, both at the low ‘drought’ end on the left and high ‘pluvial’ end on the right.

The relative accuracy of these projections indicated a greater potential for using the solar activity precursor in forecasts spanning meteorological to climatological time scales. Accordingly, the study also challenges widely-adopted published assertions[1–3] that solar forcing over climatological periods is neither evident nor significant. Clearly the recent peak in the latest solar cycle 25 in mid-2024, was substantially larger than the previous peak in 2014, and now raises the logical question of how streams such as the Animas will soon respond, if at all.

The Wallace paper focused its projections on streamflow and a few other variables, using a rationale that streamflows were ideal integrators of overall climate across large watersheds. However, streamflow records are typically challenging to rely on as contributors for comprehensive evaluations of hydroclimate, simply due to poor continuity. This often applies even for streamflow records across the satellite era beginning in 1979. In any case, the importance of more data and more analyses regarding the greater hydrosphere from the oceans to their depths and from the atmosphere to its upper water-bearing limits have long been recognized. Accordingly, a series of solar correlation mapping exercises are applied to meteorological variables which feed or influence streamflows. In contrast to the original streamflow exercises, this geospatially continuous approach provides different but supporting insights which are developed in subsequent sections.

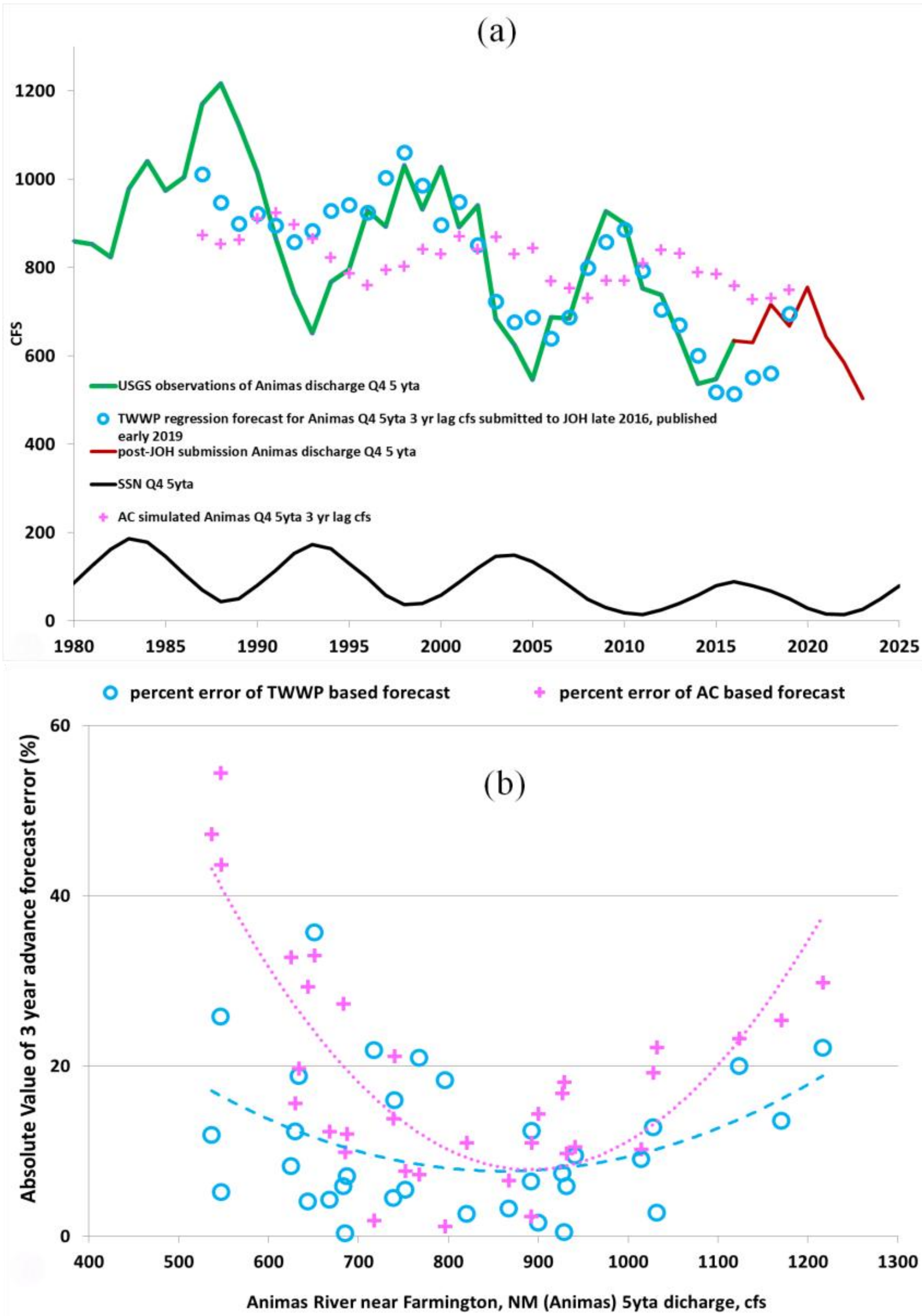

Figure 1. (**a**) Time series of 5yta solar activity (SSN, sunspot numbers) in black and flow discharge for the Animas River (green and red). (**b**) Percent error vs. Animas discharge for the CRMA and ARMA exercises.

Note: CRMA projections are open cyan circles. ARMA projections are magenta crosses.

Source: USGS 09364500 Animas River near Farmington. And SILSO for SSNs.

3.3. The Chevron Pattern of Positive and Negative Correlations of Hydrospheric Variables to Solar Activity

We noted earlier that our attention is directed at sub-global scaled parameters in relation to solar activity. First and foremost, our featured energy tracing is informed by changes in the UCAR reanalysis parameter "divergence of latent heat" (LEDIV). We interpret that LEDIV relates to Hamiltonian mechanics which naturally transforms from a Lagrangian energy balance for the dynamic moist atmosphere at any scale. This conformance is suggested, with some interpretation, from Equation (2) and **Figure 2**, which map the calculated average divergence of total heat TEDIV (**Figure 2a**) and of LEDIV (**Figure 2b**) and some orthogonal zonal circulation indicators through streamlines.

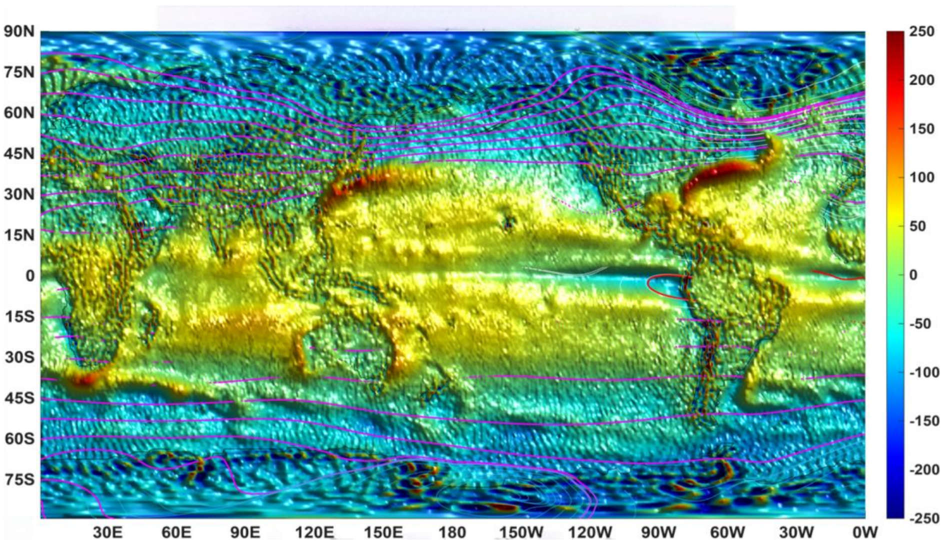

(**a**)

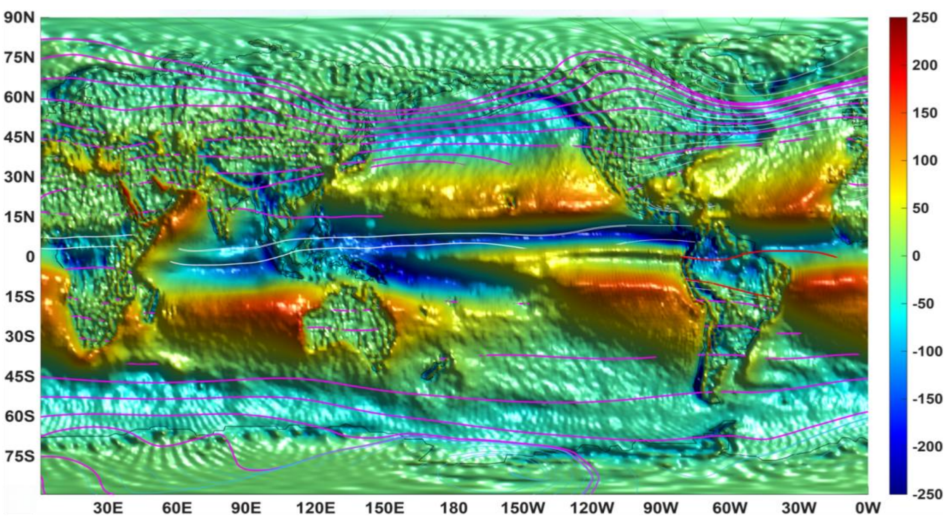

(**b**)

Figure 2. Maps of the average divergence of energy for the planet over 1979–2014 (W/m^2). (**a**) Average divergence of Total Energy (TEDIV); (**b**) Average divergence of latent energy (LEDIV).

Source: UCAR records 36-year span 1979 through 2014.

These maps were developed from the UCAR resource[18], which integrated all variables out to 100 km in elevation, beyond the upper limit of the stratosphere. The images were plotted as shaded colored surfaces, crossed by geostrophic stream 'tubes' released from 110W, to enhance the comparison between net kinetic energy and divergence of latent energy. The tubes generally representing eastward paths are colored magenta and the (generally) westward flowing paths are colored white. See Boer and Sargent [36], for an earlier and more exhaustive mapping of a wide assortment of vertically integrated energy and related mass budgets.

The map of TEDIV can be interpreted to capture the broad patterns of Earth's total energy balance and accordingly is aligned to widely accepted energy dynamics equations, which are simplified for water vapor in the equation for moist static energy (M) by Chavas and Peters [37]:

$$M = gz + C_pT + L_vq_v \qquad (2)$$

Where g is acceleration due to gravity and z is the geopotential height above mean sea level. The product of these two terms defines the potential energy of the moist air mass. The next product of C_p, the specific heat capacity of air multiplied by T the temperature of air, defines the sensible energy of the air mass. Together those first two terms define the dry static energy of the air mass. The final term is the product of the specific heat of vaporization L_v of the moist air mass and its specific humidity q_v.

TEDIV is a summation of the latent heat divergence and the sensible heat exchanges (captured through dry static energy). Because they are represented as integrated divergences, they are interpreted as fluxes of energy towards or away from the planet's surface. These heat traces are independent of other representations of radiative heating and cooling. Notably both components are orthogonal to geostrophic circulation components, and that vertical simplification is a characteristic shared by radiative heating in the contributions of each to the total energy balance of the Earth. In particular, the polar regions shaded in blue of the TEDIV map signify the net release of sensible heat into outer space via radiation from the surface as well as the thin atmosphere there. In contrast the broad yellow fields reflect tropical and subtropical impacts of evaporation and condensation and sensible heat transport presumably via eddy diffusion. The evaporation and condensation components are more clearly indicated in the LEDIV map of **Figure 2b**. Red zones there reflect regions of highest production of latent heat due to evaporation over watery surfaces. The blue zones indicate regions of highest removal of latent heat from the atmosphere due to condensation at upper levels of the hydrosphere (typically considered as the tropopause at approximately 12 km elevation).

The LEDIV map in **Figure 2b** again draws attention to the intense zone of intertropical convergence (ITCZ) in blue that aligns closely to the equator. As noted, the blue bands signify condensation, and thereby the release of latent heat in the upper atmosphere. It is interesting that the absolute magnitude of LEDIV there appears to meet or exceed 239 W/m^2, which is the average solar radiation bathing Earth according to Gray et al. [1]. In addition, roughly matching in magnitude but opposite in sign, the red LEDIV mounds include a distinctive wedge above the Peru Current, which is well known as a major transport route for cold Southern Ocean waters to reach equatorial latitudes in the Pacific Ocean. This wedge of high positive tropical LEDIV aligned with eastern rims of the Pacific, Atlantic and Indian oceans is moreover a contributing element of the chevron pattern featured in this section.

It is true that lateral latent energy transports are described in WG1AR6 Section 7.4.4.1 as important candidates for causation of "polar amplification" of global warming. On the other hand, that mechanism is disconnected from solar activity and instead shares space with greenhouse gas causality, according to their modeled paths. From a relative perspective, LEDIV across the tropical surfaces actually dominates the energy balancing. **Figure 2b** for example explicitly shows that LEDIV energy exchanges routinely approach the maximum solar energy that reaches the planet. The dominance and dynamics of equatorial LEDIV in the global energy balance are not extensively discussed in climate literature. For example, latent heat is not treated in the Gray et al. paper. And, as previously described, latent heat is only indirectly accounted for within GCMs as inert parameterizations. In contrast, the LEDIV surface uniquely and dynamically informs our exploration of solar correlation, particularly for the moist atmosphere.

In particular, as demonstrated in the following and later examples, solar correlation patterns are always expressed as paired and roughly symmetrical domains of relatively high negative and positive values. Based on this understanding, we explored such solar correlations to specific humidity, specific rainwater content, geopotential height, surface temperature, percent of cloud cover, and specific snow water content above the ocean surface and temperature, vertical velocity and salinity below the surface. Note that "specific" indicates the value is a mass fraction for each volumetric cell of the source data reanalysis product. As a starting point, **Figure 3** maps the principal solar correlations and related trends found in this study to several major variables: surface specific humidity Q at the top, surface temperature T in the middle row and near-surface seawater temperature at the bottom row. In addition to the SILSO reference for solar activity (i.e., sunspot numbers), each image derives the variable of interest from widely used reanalysis datasets. The top two images come from the ERA5 surface reanalysis datasets covering a time period of 47 years, from 1979 through to the end of 2025. The bottom image is developed from NASA ECCO records for ocean temperature reanalyses from the years 1992 through 2017. **Appendix A** contains details for each data source in this study.

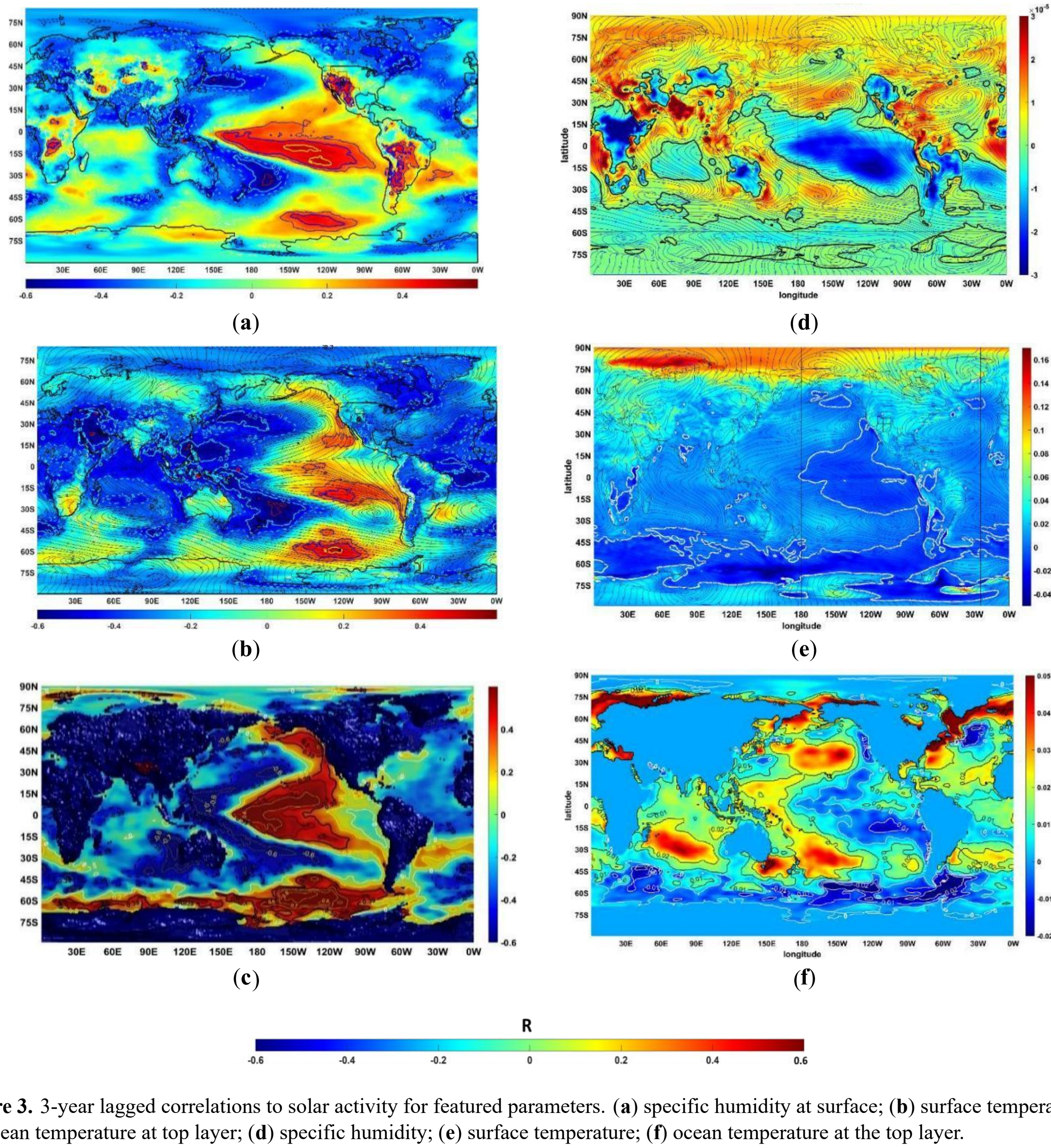

Figure 3. 3-year lagged correlations to solar activity for featured parameters. (**a**) specific humidity at surface; (**b**) surface temperature; (**c**) ocean temperature at top layer; (**d**) specific humidity; (**e**) surface temperature; (**f**) ocean temperature at the top layer.

Sources: ERA5 and NASA ECCO.

It is notable that for each solar correlation case, from north to south, crossing the Pacific and extending from the shallow ocean through the lower atmosphere, a chevron pattern of positively correlated regions in red along the east, dovetails into negatively correlated regions along the west. The magnitudes of the positive and negative correlations of each variable with solar activity appear roughly balanced. The central image includes a surface overlay of streamlines representing the average atmospheric surface circulation. That wind circulation also aligns well with the chevron boundary, helping to establish that the boundary is related to circulation as well as latent heat. Possibly, the state changes in the hydrosphere due to latent heat as described here can account for the sign changes in the correlations of many climate parameters with solar activity across the chevron boundary.

Moreover, these contrasting signs of the correlations and affinities to circulation appear to align well and expand upon the dipoles described by Xiao et al. [32], and Huo et al. [33]. Those studies identified a dipole signature over the "tropical western Pacific" for the 2-year lagged correlation of solar activity to outgoing longwave radiation (OLR) for the boreal summer (Xiao et al.) and to ocean heat content (Huo et al.). The OLR correlation was also found to align with a convection dipole at the same location. Furthermore, these alignments to the extended chevron pattern featured in our current study suggest that Xiao et al. and Huo et al. identified the apex of a correlation and circulation dipole, centered around the WEP, and may be most intense at the ocean surface. Once the dipole chevron pattern is considered, other patterns appear to align. For example, Figure 6 of Smyth [38] captures the same chevron pattern in their examination of 4 bandwidths of UV and the penetration of the longer wavelength bands to penetrate nearly over 70 m into the ocean. Finally, in alignment with the Hadley Cell limits, the chevron pattern extends towards each pole but then is blocked to some extent by the well-known obstacles and diversions including land masses and polar circulation cells. It could be interpreted that the chevron dipole is a roughly symmetric "crease" in the Hadley Cell that signifies changes in both the state and circulation of water.

Based on the trends of each variable in **Figure 3**, we interpret this as significant because the trends are not controversial even if the correlations are found to be. Currently, neither the chevron patterns in trends and solar correlations, nor the LEDIV maps of the state changes of the global hydrosphere appear to be extensively featured in previously published literature, although the chevron pattern is evident in numerous global climate maps. The surface trend maps are in this case based on the ERAI data series which ran from 1979 through 2018 (40 years).

The correlations in **Figure 3** are shown for the third year of lag, which is the lagged year with the highest solar correlations among the featured variables. **Appendix B Figure A1** includes additional global scaled maps of correlations investigated for each of the parameters of **Figure 3**, but now covering each featured lag from 0 (i.e., no lag) to 5 years. Notably, for **Figure 3c**, the lagged correlations of near-surface ocean temperature to solar activity after three years are stronger than the surface (atmosphere) equivalents in **Figure 3a,b**. Finally, it is again notable that the magnitude and signs of solar correlation appear to roughly match the documented trends. This is evident for each row. For example, in the top row, the east equatorial chevron in red hues of specific humidity in **Figure 3a**, reflects high lagged positive solar correlation. And for the panel to the right at **Figure 3d**, the index color within that chevron zone is deep blue, representing a decreasing trend in the same specific humidity parameter. This is the expected trend direction because solar activity had trended down over the reference time span, as evident from **Figure 1**. The same observations apply for the second row for the same reason: **Figure 3b** shows a strong positive correlation of surface temperature in the eastern equatorial wedge via the deep red hue, while its counterpart in **Figure 3e** shows a corresponding downward trend by the deep blue eastern equatorial wedge. Finally, in the bottom row of **Figure 3** the east chevron zone of high solar correlation (**Figure 3c**) of near-surface ocean temperature correlation to solar activity (red hue), matches the same east footprint for a cooling trend shown in **Figure 3f**. The reason is again the same as noted for the previous rows, that solar activity has declined over this same period.

Furthermore, this chevron zone encompasses and expands on the entire ENSO footprint. ENSO is understood to be sensitive to cooling waters in this footprint, and it is equally understood that short-term climate around important synoptic regions of the world is sensitive to ENSO. But there is little solar attribution in the literature aside from Kodera [39]. which described lagged monthly correlations greater than 0.6, between solar time series and the ENSO footprint. The lack of connection studies between ENSO and the solar cycle may be why most relevant researchers continue to consider ENSO a separate variable. Notably even

Xiao et al.[32] purposefully filtered out ENSO and yet still found a solar correlation equatorial dipole. The importance of ENSO is not underestimated in our study or ongoing work. But we note its solar chevron-aligned footprint and that its scale and the scale of interest in this study are different, and accordingly, so are many of the expected applications.

3.4. Ocean Solar Correlation Patterns Dovetail to Atmospheric Correlations

These observations justified in our context an expanded exploration of ocean circulations by relying on additional datasets of the ECCO record set, including velocities and salinities, as featured in all panels of **Figure 4** and described subsequently. These connections are primarily interpreted in this study to relate to latent heat dynamics of the climate system as well as sensible heat transport through the ocean from the Antarctic towards the equator via the Peru Current. Typically, in these examples, areas of positive solar correlation suggest cooling and drying simply because solar activity has generally diminished until recently in the nearly 5-decade-long record considered and because those regions have not been altered (as extensively as elsewhere) via moisture state changes. For purposes of this exploratory examination, we remain focused on transport of latent and sensible heat but in ways which should inform subsequent studies by any interested researcher.

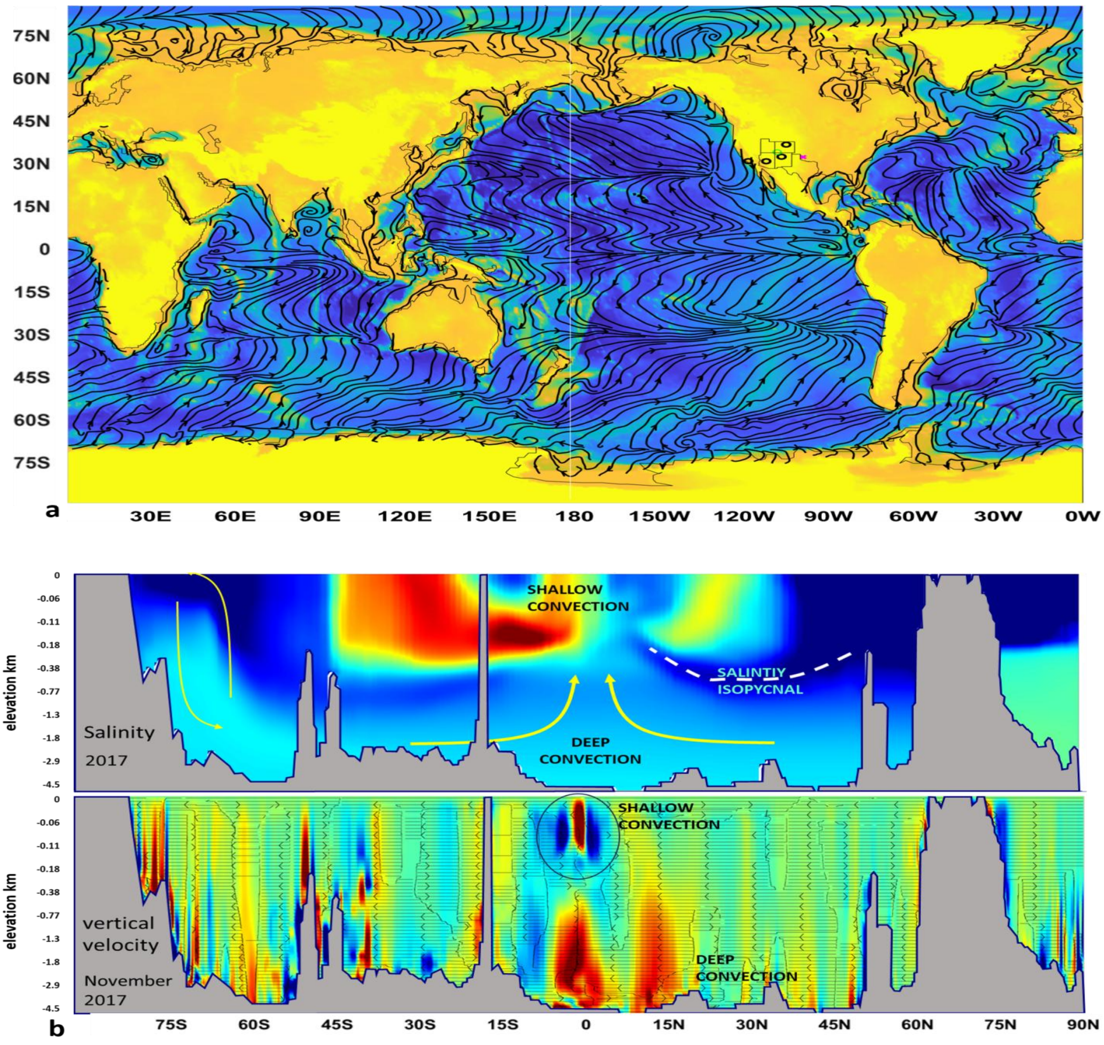

Figure 4. (**a**) Map of average shallow ocean velocity (layer 49 of ECCO records) streamlines for year 1993 overlain onto the planetary topography including that of the ocean floor (color). (**b**) Top: vertical profiles of ocean salinity for example year 2017 stacked over bottom: vertical profiles of ocean vertical velocity component for same year and meridian.

Note: Vertical line represents the 180° E/W meridian used for the profiles of **Figure 4b**.

To explore further aspects of the ocean datasets for salinity and velocity in the ocean, we surveyed key layers and transects through the geospatial data sets. **Figure 4** provides two examples. In the layer map of **Figure 4a**, the Earth's solid surface relative elevation is shown by the color field, overlain by ocean velocity streamlines in a near-surface layer (49 of 50). At this depth and below, the streamlines show conformity to the underlying bathymetry. Ocean circulations are well understood in many respects, but we found the alignment to the underlying surface interesting in our context. Accordingly, we followed up with the stacked profiles of **Figure 4b**. These are both taken along the 180° E/W transect, which is shown as the white line in **Figure 4a**. This cross section notably applies to the world's dominant ocean basin, the Pacific, which is the largest unobstructed ocean surface on Earth, extending nearly from pole to pole like the Atlantic, but twice as wide. Notably, the Pacific Ocean nearly occupies an entire hemisphere.

Viewed across the middle of the Pacific Ocean from pole to pole, the profile in **Figure 4b** for the example month and year of November 2017 illustrates a pole-to-equator overturning pattern in salinity that resembles simple convection, similar to the overlying atmospheric Hadley Cell. Moreover, the Pacific Ocean salinity patterns are also significantly lag-correlated to solar activity, much like the other featured parameters. This is indicated in the six plates of **Figure A2**. Those capture the lagged correlations of the near-surface ocean layer of salinity to sunspot numbers, following the same setup as the previous figures for ocean temperature-lagged correlations to solar activity.

The lower panel of **Figure 4b** shows the patterns in vertical velocities of the global ocean for the same featured month and year, November, 2017. Notably, several areas indicate vertical plumes emerging from the ocean floor. The key region of vertical convection is evidently along the equatorial ocean floor for this example month, where two significant 'plumes' are indicated in red. A secondary region of increased vertical velocity lies along the Southern Ocean/Antarctic coast slope. Another area of interest appears at the shallow equatorial zone. These are only selected profiles of selected variables over one month and are intended to be illustrative.

However, they also lead to numerous additional questions, including in particular, the appearance of what the two panels of **Figure 4b** term "deep convection".

Although the maps are not included in this study, other months show a wide range of intermittent deep convection patterns. But unlike those zones along the ocean floor, a more persistent and stationary convection seems anchored to the ocean's shallow pelagic layer, labeled here as "shallow convection". We note that for these compressed profiles, the pelagic zone of the ocean is the depth from 0 to 200 m, where solar radiation can be utilized by phytoplankton for photosynthesis. Because of the conventions of the ECCO dataset and our graphic adjustments, the vertical scale of this zone is enlarged to fill the top third of these profiles, which ultimately extend down to ~5 km in depth. Accordingly, this shallow equatorial ocean convection zone fits well with our understanding of the depth to which solar radiation can nominally reach. Notably in that context, pelagic phytoplankton play a critical role at the root of almost all ocean biomass [40]. And all deceased biomass (detritus, also known as marine snow) reaches the ocean floor as solid matter relatively rapidly and continuously. See for example Barton et al. [41] for a review of the relevant literature.

Shallow convection is recognized by other studies including Vreugdenhil and Gayen [42], which report open ocean convection thousands of meters deep. In a relevant preceding work, Nilsson and Körnich [43] noted an "Oceanic Hadley Cell" and demonstrated this by stacking the atmospheric Hadley humidity profile over the ocean salinity profile. Unlike greenhouse gas causal models, coupled atmosphere-ocean models, including the one used by Huo et al. [33] directly incorporate solar forcing and related latent heat dynamics. This approach stems from their closer connection to short-term weather models, which routinely account for solar radiance and latent heat production and consumption in projection exercises and notably, disregard greenhouse gas radiative forcing. This added attention may account for the insight into the stacked Hadley Cell. Coupled Atmosphere Ocean Models (CAOMs) have even investigated solar forcing effects on ocean levels as deep as 1 km as already noted in regard to Vreugdenhil and Gayen [42].

The penetration of solar radiation into the abyssal ocean is not widely considered plausible, given measurements at depth, UVA-visible in situ and remote sensing techniques, and analytical calculations (for example see Lee et al. [44]). That tremote-sensing application study suggest an average euphotic depth to be at least 70 m. Other general information sources such as the National Ocean Service at https://oceanservice.noaa.gov/facts/light_travel.html, indicates that sunlight can be detected as deep at 1,000 m but that photosynthesis cannot generally occur below 200 m.

Global ocean overturning is acknowledged in the literature by Döös et al.[45], but it has not been thoroughly linked to convection, except indirectly through studies on horizontal convection, such as Gayen and Griffiths[46], and siphoning, as described by Monismith et al.[47]. Accordingly, much remains to be sorted out about convection features in the abyssal zone, and alternatives to direct solar radiation of the ocean floor seem to merit initial consideration. We entertain such a notion in regard to sedimentation of ocean biomass. The constant sinking of biomass, along with the release of chemical energy of this biomass after biodegradation on the ocean floor may be signified by those deep temperature—solar correlation plumes, if for no other reason than that solar radiation is accepted to drive the growth of all biomass, starting with phytoplankton, and falling biomass brings surface warmth along, perhaps in sufficient quantities to account for the observations in this study.

Again, convection is generally understood to occur in a fluid when heat is applied at the bottom of the supporting surface. Heating causes buoyancy effects, which trigger the rise of warmer fluid parcels. As these parcels rise, others fall or transfer from the sides, making the system roughly diapycnal and diabatic, in line with traditional convection. **Figure 5** and others that follow were developed to help resolve some of these questions by again featuring lagged solar correlations, but now applied to vertical velocity, temperature and salinity across the same Pacific profile.

The ocean vertical velocity variable is featured in the first column of **Figure 5**, but now as an average annual time series that is correlated to the annual SSNs by lags from 0 (top) to 5 years (bottom). In our interpretations, circulation features can be inferred from the progress of concentrations (or parcels) of high negative and positive correlations. And they can be corroborated through review of streamlines as desired. Notably the deep convection features at the equatorial ocean bottom in the previous **Figure 4** are not evident but other areas to the north and south show solar correlations to the bottom of the ocean. Perhaps more notable is that the central shallow convection feature, which is itself possibly stationary, shows a lagged response to solar activity according to the same time frame and progression as the previous examples.

Annual SSNs always swings between an intensification phase and a diminishment phase within each roughly 11-year repeating (cycling) period. The shallow ocean convection system "responds" (is significantly correlated) the most by the third year of lag. The middle column of **Figure 5** addresses the same lags of correlation for temperature across the same profile. An even broader shallow convection zone seems evident, along with a significant proportion of the Southern Ocean's pelagic zone along this profile. First, it seems apparent from the positive and negative boundaries, especially over the 3rd and 4th years of lag solar activity rises, the core temperature of the equatorial pelagic zone rises and the surrounding tropical/subtropical bands cool. And as Solar activity declines, the core T drops and the surrounding T rises. This is explored further in the subsequent figures.

Moreover, significant zones of solar-correlated temperature are also evident in abyssal waters. Our discussions earlier traversed the concept of deep convection and it is tempting to consider these abyssal correlations as related. However, the abyssal vertical velocity graph featured in **Figure 4b** is not a stationary feature, while the temperature correlations at the same depths persist from month to month and year to year, so far as we have examined. As an alternative explanation, we continue to consider the sedimentation notion, i.e., the informal postulate that the sinking of biomass synthesized in the photic zone and the chemical energy release through biodegradation at the bottom of the water column brings the surface solar temperature correlation down with it. We already can interpret a corroboration in the middle column of **Figure 5**. The sequence of lags from 0 to 5 years featured from top to bottom indicate that solar correlation to abyssal equatorial pacific temperatures emerges by the third year of lag, but then appear to stabilize to a statistically-significant level. The final column of **Figure 5** again covers the same lags but now for the salinity variable. Notably, the variations in correlation, both negative and positive, intensify and decay over the multiyear period. Moreover, the connections of positive and negative values appear to align with the observations of Nilsson and Körnich[43]. Those authors noted a band of high subtropical surface salinity on both sides of equator roughly in line with the top of the salinity profile in **Figure 4b** and in the correlation maps in the final column of **Figure 5**.

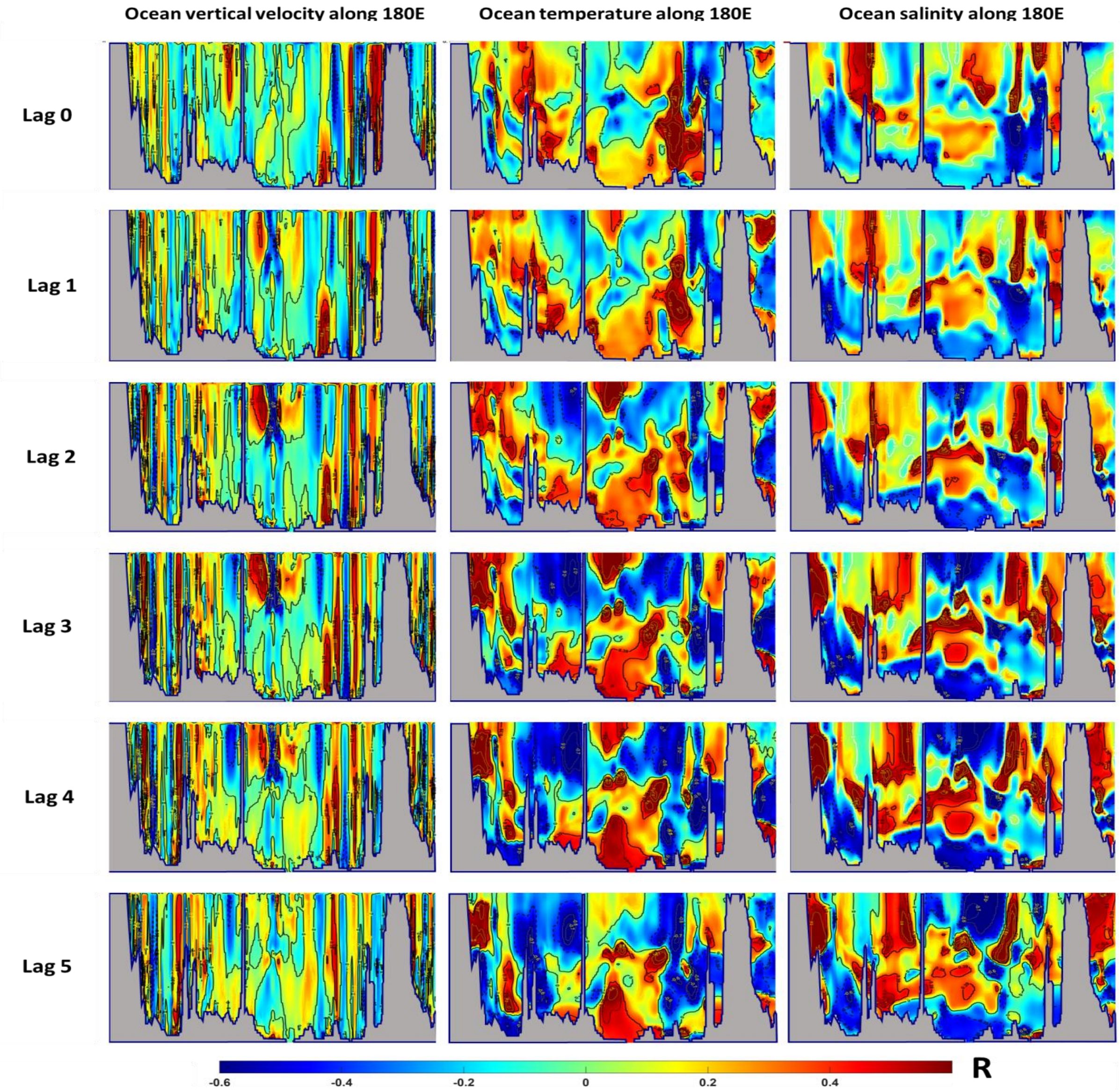

Figure 5. Ocean profiles along 180° E of lagged solar correlations to vertical velocities (left column), temperature (center column) and salinity (right column). Lags from 0 years (top row) to 5 years (bottom row).

There are additional notable features in the temperature and salinity correlation columns, especially for the early half of the lagged series. High positive correlations to solar activity might arguably appear as plumes that rise from the tops of some of the profiled abyssal—rooted hills. This is only a qualitative interpretation and invites further consideration of the impacts of falling biomass. As noted by Durden et al.[48], "megafaunal biomass" appears to concentrate over these peaks. Whatever mechanisms may connect biomass to solar correlation might need to be disambiguated from among other candidates, including geothermal features, which also are known to be associated with abyssal peaks. For example, the work of Kim et al.[49], features a study of geothermal vents associated with the Central Indian (subterranean) Ridge.

Finally for this initial interpretation it is convenient to compare Column 2 to Column 3. For most of the profiles from the upper abyss to the surface, the two variables of temperature and salinity both positively correlate to solar activity. But across the equatorial bands, the abyssal temperatures positively correlate while the abyssal salinity negatively correlates. This motivates our responsive and qualitative interpretation that in addition to thermally significant properties of biomass sedimentation, they also may entrain significant fresh water from the surface on their rapid descent.

Again, these are qualitative initial interpretations. Clearly the featured patterns of correlation invite further study beyond this initial exploration. As noted, our parallel studies consider some related information but for now, we consider a few additional complementary patterns that seem most relevant towards roughly completing the basic limbs of our concept of a solar driven 'Super' Hadley Cell. The patterns of the five stacked variables in **Figure 6**, the 1992 ocean atmosphere CO_2 flux map in **Figure 7a**, and the related two stacked variables of **Figure 8** as examined vertically and horizontally, suggest a relatively unified conceptual model of solar activity—driven ocean and atmospheric circulation of moisture, dry air, and CO_2. These concepts are explored in further detail subsequently. For now, the results are paired together to show a number of interesting alignments.

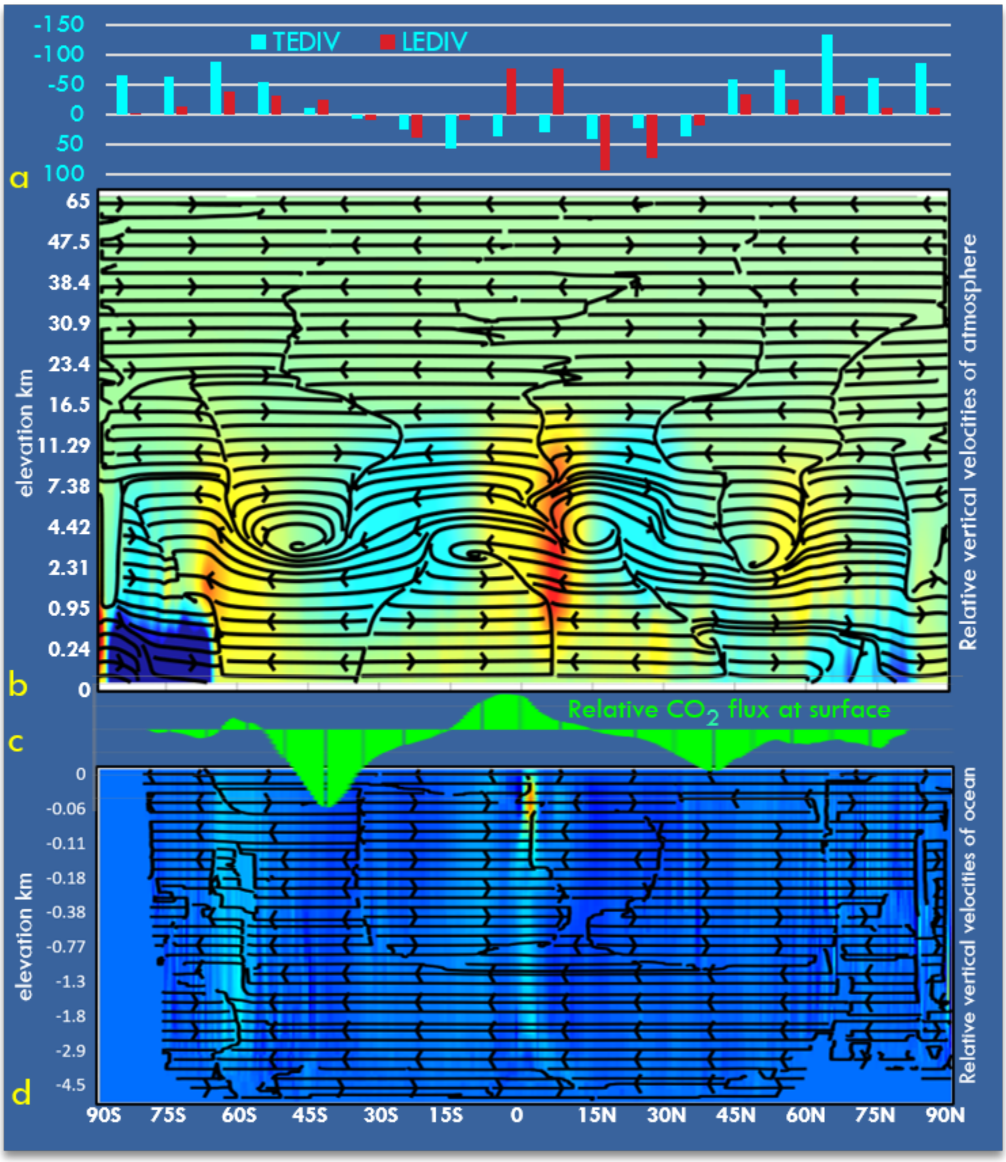

Figure 6. Global profiles of atmospheric and ocean features. (**a**) Divergence of Latent and Total Energy (LEDIV, TEDIV W/m^2) 1992 profile along 180° E; (**b**) Zonal average atmosphere vertical velocity (color field, red = strong upward magnitude, blue = strong downwelling range) and stream slice overlay, (1992); (**c**) Zonal average ocean-air CO_2 relative flux histogram (1992); (**d**) Zonal average ocean vertical velocity (color field) (color field, red = strong upward magnitude, blue = strong downwelling range and stream slice overlay (1992).

Source: UCAR, ERAI, MPI, ECCO.

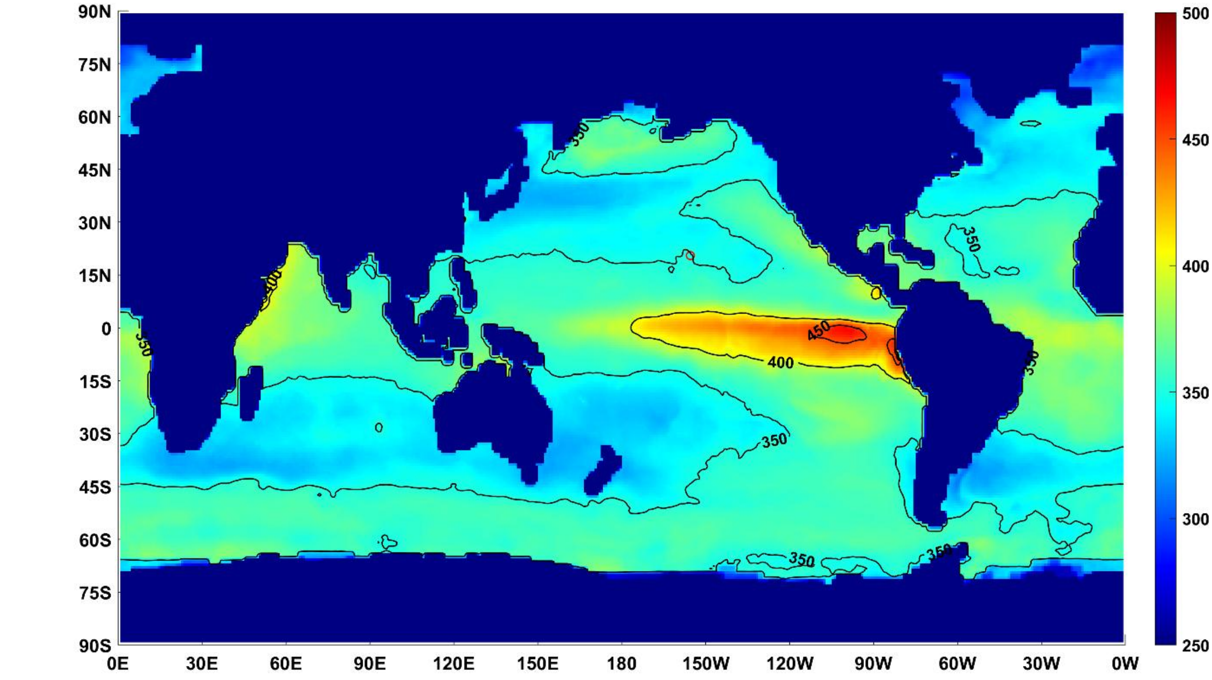

(**a**)

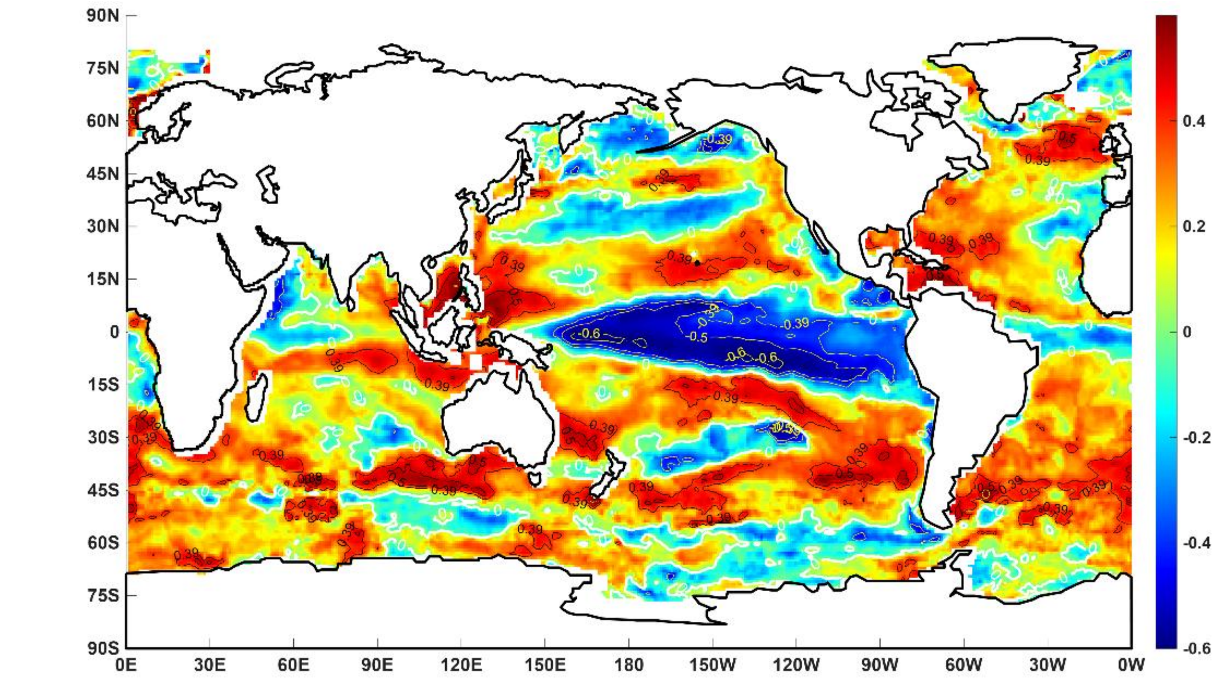

(**b**)

Figure 7. Ocean-atmosphere CO_2 concentration and flux data. (**a**) Average CO_2 concentration (ppm) at ocean surface, years 1982 through 2017. (**b**) 3-year lagged correlation of CO_2 flux at surface (mol/m^2/year/month) to the sunspot number series for the same 1982 through 2017 time frame.

Source: SILSO, and Landschützer et al. [21] incorporating SOCAT and SOCCOM data.

For example, **Figure 6a** displays histograms of the net fluxes over the given year of 1992, for total energy (TEDIV) and latent energy (LEDIV).These align with each other and with the equivalent geostrophic maps of each in **Figure 2**. Consistent with our earlier interpretation, the greatest release of latent heat to outer space occurs near the equator from the tropopause, and this is captured geostrophically (without a specific elevation) by the tallest red bars of **Figure 6a**. Moreover, the tallest cyan bars (TEDIV) indicate that the subpolar and polar zones dominate in the transport of otherwise sensible energy to space, and this is also corroborated by **Figure 2a**.

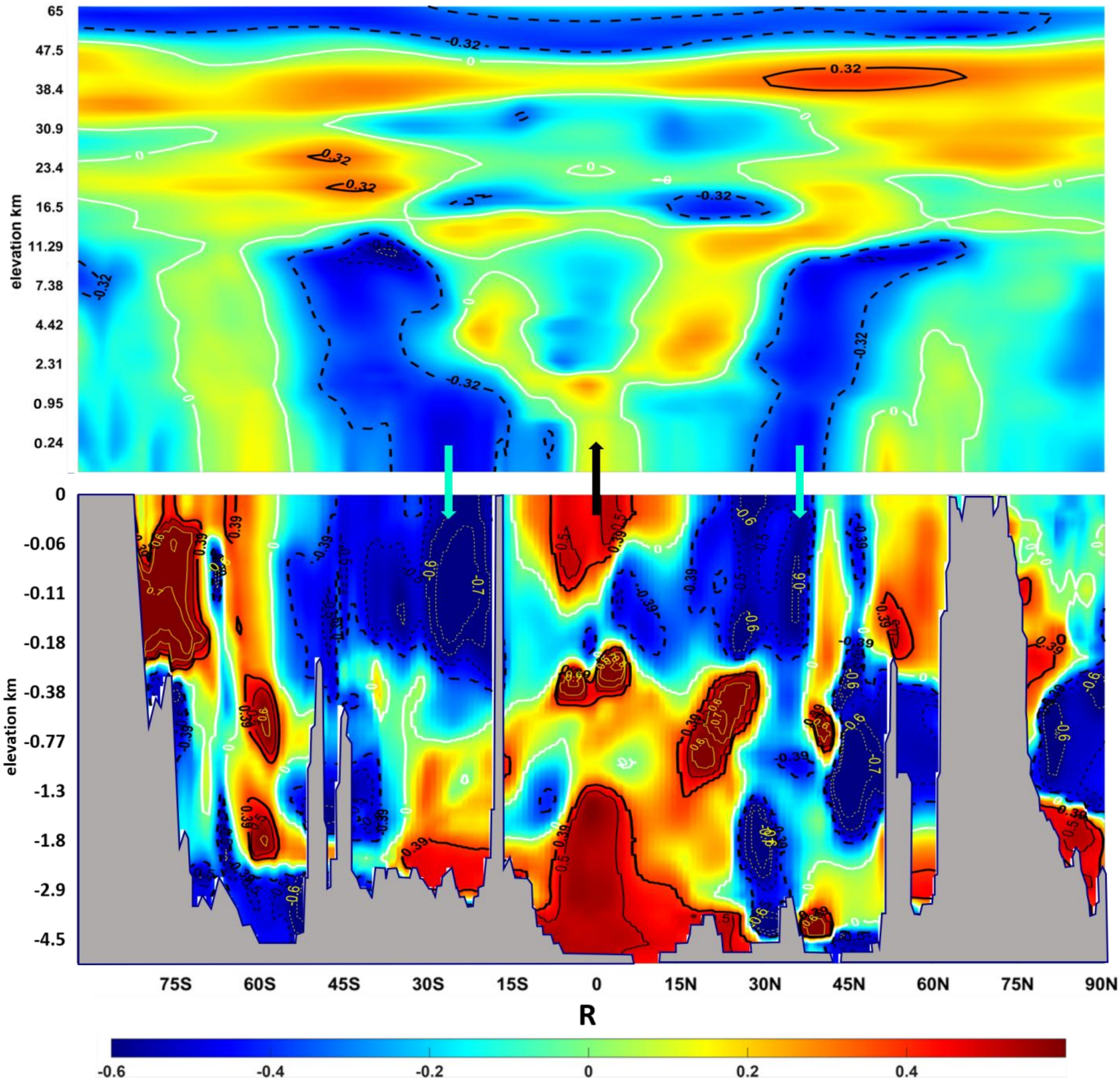

Figure 8. Stacked profiles at 180° E of 4-year lagged correlation of atmosphere T (top) and ocean T (bottom), with solar activity.
Note: Cyan arrows indicate downward bands of cold liquid water. Black arrow shows upward band of water vapor.
Source: ERAI, ECCO.

These divisions of outwardly diverging energy from the latent and sensible components are naturally non-controversial. Yet the radiative balance of the atmosphere is rarely characterized this way in the associated literature [1–3]. For example, as noted the WG1AR5 reference [2] never explores latent heat other than as an input, and "sensible heat" as well as "dry static energy" are not described. Radiative forcing in the perspective of the D&A community is primarily about negative forcings that adjust solar radiation but almost never directly about solar radiation itself. It is true that the literature [2] includes a Section 8.6.1, on the spatial distribution of some climate forcing agents including CO_2, aerosols and ozone. But the "Solar irradiance" forcing factor is not included in that discussion.

Also, the full panel set indicates that regions of positive and negative vertical atmospheric and ocean velocities (rows 2 and 4) align with regions of negative and positive LEDIV in the upper row, and with regions of positive and negative CO_2

ocean atmospheric flux (green vertical bar chart) in the third row. This fits with our existing interpretations associated with **Figure 2**. The CO_2 flux histogram is also comparable to the map in **Figure 7a** of the mean equatorial upwelling and mid-latitude downwelling of CO_2 for the full set of years available from the MPI resource (1982–2017). This data was drawn from Landschützer et al.[21]. Both the CO_2 relative flux histogram in **Figure 6c** and the CO_2 concentration map of **Figure 7a** align with the bottom panel of Figure 5 of Carroll et al.[50], and this is discussed further in subsequent paragraphs.

Perhaps most notable is the significant (negative) correlation of equatorial CO_2 upwelling with solar activity that is clearly mapped in **Figure 7b**. Moreover, positive bands of correlation bound this domain to both north and south. The positive bands are aligned to the downwelling CO_2 indicated in **Figure 6c**, from the same source. CO_2 circulation is described in more detail along with another tracer in a subsequent section.

That CO_2–solar correlation map is complemented in **Figure 8** with two stacked profiles of additional solar correlation interest. The figure shows that regions of positive and negative solar correlation to temperature at any depth in the ocean or elevation in the atmosphere align roughly at the atmospheric ocean interface. The cyan arrows and black arrow in **Figure 8** illustrate important aspects of our interpretation of sensible heat transport. Cyan arrows reflect the cooling of the atmosphere and ocean from first the subsidence of cold water and frozen precipitate condensed from vapor at high altitudes. The precipitation reaches the ocean surface and cools its ocean surroundings as the meteoric water sinks. The black arrow reflects the production of water vapor across the equatorial core surface above the shallow equatorial convection zone, and its transmission to the atmosphere. That adds significant quantities of latent heat which are interpreted further to be captured by the yellow and orange lobes of **Figure 2b**.

Moreover, the alignments of negative correlation are stronger than the alignments of positive correlation at this "late" lag of 4 years. Also, it is of interest that the same figure demonstrates the significant correlation of the temperature of the ocean floor to solar activity even after 4 years, as signified by the extensive deep red zones. That lower half of the figure is an enlarged version of the 4^{th} row of the middle column of **Figure 5**. Finally, the same bottom frame of **Figure 8** also demonstrates a shallow equatorial zone of high positive solar correlation which aligns with the shallow zone of ocean convection featured in **Figure 4b**.

4. Discussion

The numerous connections already featured complete a core set of observations and related analysis. But they can be augmented further by (and augment in turn) additional geospatial evidence regarding both CO_2 and O_3. We discuss both of these atmospheric and/or ocean tracers in some depth here, not only because they are helpful to expand upon the hydrospheric components and dynamics already described, but also because both are key forcing parameters featured in the WG1AR5 and WG1AR6 reports.

Following this discussion, our analysis integrates all of the featured tracer and hydrospheric information to build an alternate conceptual model of the geospatial impact of solar activity upon the planet, namely the "Super" Hadley Cell. The discussions are closed with an example forecast to test the predictability of the featured lag correlations.

4.1. CO_2 And O_3 Patterns Align to the Hydrospheric Circulation Model

In following up from the largely hydrospheric parameters featured, we have also examined geospatial products for the trace gases CO_2 and O_3. Both are reviewed for several reasons. First, they are described in previous literature with varying chemical connections, and via more correlations, to either the hydrosphere or to solar or both. For example, atmospheric CO_2 transport that aligns seasonally with the HC is clear from numerous figures and related text from Miyazaki et al 2008[51]. And second, both tracer gases are important in the WG1AR5 and WG1AR6 model global forcing hierarchy. Notably as summarized in **Table 1**, solar forcing again occupies the weakest position of that hierarchy.

Table 1. Selected global radiative forcings (W/m^2) reported in WG1AR5 by Myhre et al.[2].

Forcing Parameter	Mean Value (W/m^2)
Carbon Dioxide (CO_2)	1.82
Methane (CH_4)	0.48
Tropospheric Ozone (O_3)	0.4
CFCs	0.263
Nitrous Oxide (N_2O)	0.17
Stratospheric Ozone (O_3)	−0.05
Solar Activity (SSN)	0.05

CO_2 occupies the top forcing ranking, followed by numerous additional trace gases (some not included in this excerpt), before the solar forcing minimal value of 0.05 W/m^2 is recognized. Each of those additional gases shown is related in WG1AR5, WG1AR6, and supporting literature in some manner to ozone, as subsequently described.

Accordingly, additional examination of both CO_2 and O_3 serves multiple comparative purposes regarding the notion of solar forcing's impact upon our hydroclimate. For example, CO_2(g) is heavier than air but lighter than H_2O(l) into which it can fully dissolve. O_3(g) is also heavier than air and is soluble in water. In addition, CO_2 pathways cycle between the ocean and the troposphere, while O_3 originates in the stratosphere and descends through the troposphere to the surface.

4.2. CO_2 Fate and Transport in the Hydrosphere

The CO_2 mapping featured in **Figures 6c** and **7a** comes from two atlases of dissolved CO_2 fugacities, described in detail by Landschützer et al.[21]. The SOCAT atlas covered data north of the Southern Ocean and the SOCCOM atlas covered the data within the Southern Ocean footprint. Clearly the CO_2 concentrations are greatest over much of the equatorial Pacific, and lowest along the middle latitudes of the Pacific. This is also supported by Figures 12 and 15 of Miyazaki et al.[51]. All reports and data that we examined showed that the greatest mass of CO_2(g) emerges into the lower atmosphere, mainly from the equatorial Eastern Pacific, from which it upwells and degasses. Once in the atmosphere, CO_2 follows atmospheric circulation patterns, including the Hadley Cell (HC) (see Miyazaki et al.[51] Figure 15 and more again). CO_2 concentrations are observable with downward (nadir) viewing sounder approaches focused on the mid-troposphere[52].

Nonetheless CO_2 is understood to uplift through the tropical tropopause much like H_2O. Because there is no condensation loss, CO_2 concentrations within the stratosphere can be expected to remain less depleted than H_2O. Eventually, within a few years of residency, the CO_2 returns to the ocean and land surfaces through both wet deposition along the mid-latitude descending limbs of the HC, and to the north via the Brewer-Dobson circulation.

Much of this description is adapted from Bischof et al.[53] and Andrews et al.[54]. Both studies included globally scaled integration of stratospheric observations, including from high-altitude aircraft and "balloon-born cryosamplers". The Bischof study interpreted that most stratospheric CO_2 originates from the tropical troposphere, via upwelling. They also observed a slight drop, ~ 7 ppm(v), around 2% of the tropospheric average, in stratospheric CO_2 concentration from the tropopause to the middle of the stratosphere. The Andrews study developed a model using Green's Function to build the case for the transport patterns and the residence times of stratospheric CO_2 and several other gases. The Hadley portions of those inferred CO_2 patterns can be inferred from both the blue-shaded mid-latitude zones in **Figure 7a** and again the downward arrows in Figure 15 of Miyazaki et al.[51].

The interpretation of CO_2 and the Hadley Cell that our study shares with Miyazaki et al. was preceded by related descriptions of an "atmospheric conveyor belt"[55]. The connections however are most clear in comparison again to our content and Figures 12 and 15 of Miyazaki et al.[51]. That paper uses stream-function-based models and improves skill transparency through extensive comparisons to observations, including reanalysis products. This is done with the goal of mapping the most likely pattern of CO_2 cycling in the atmosphere across the ocean portions of the planet.

Figure 7b advances from the previous content on CO_2 fluxes between the ocean and atmosphere to develop a map of the SSN 3-year lagged correlation to CO_2 flux. Notably, the map once again manifests as a rough meridional dipole as in previous maps (see Figure12 of Miyazaki et al.[51]). All of this information supports the inclusion of CO_2 as both a tracer of circulation and another indicator of the influence of solar forcing.

In that regard, the evidence of solar forcing of ocean-upwelled CO_2 poses an additional challenge to the WG1AR5 climate forcing hierarchy, because the weakest forcing agent cannot logically drive the strongest forcing agent. Myhr et al.'s[2] paper on climate forcings describes anthropogenic CO_2 forcing and implementation in much detail but does not point to supporting observations or sample collections that clearly disambiguate natural CO_2 from fossil fuel-related CO_2.

Regardless of where or how CO_2 is argued to be produced or destroyed, the WG1AR5 and WG1AR6 aligned works such as DeVries[56] identify an anthropogenic factor as the deciding factor, and the impacts of H_2O and solar activity are not deeply explored. In contrast, other papers such as Andrews et al.[54] and Miyazaki et al.[51] as previously noted have directly investigated and modeled at least the natural dynamics of CO_2 cycling that is heavily grounded in the primacy of equatorial upwelling. Finally, as noted, both have also authenticated against published and/or measured observations.

For completeness at this preliminary stage, we recognize that there are other sources of CO_2 fluxes to the south and north of the Hadley Cell. See example from Wu et al.[57] which features deeply penetrating ocean mixing depths across the Labrador Sea for mean March (1979–2017 span) to the west of Greenland. A complementary but more explicit treatment of ocean-atmosphere CO_2 mixing is viewable at https://svs.gsfc.nasa.gov/4398[58]. This animation for all weeks of 2009 was built within the NASA Carbon Monitoring System (CMS) Flux Project[59]. The March maps show intense subpolar North Atlantic CO_2 upwelling activity, which is also in alignment with Wu et al.[57]. In addition, the animation appears to signify the more subtropical and tropical upwelling and downwelling mapped in **Figure 7a**. Finally, the supporting text of the site notes the graphical overlay of vortices as streamlines over plumes as color fields of upwelled and down-welled CO_2 from June through November, suggesting that important quantities of CO_2 are pulled from abyssal ocean zones directly to the "free" (upper) troposphere via the eye of each cyclone storm.

Finally it is notable that these natural CO_2 signatures are not directly addressed in WG1AR5 representations of CO_2 fate and transport. Instead, only model-based representation of CO_2 accounting, both natural and anthropogenic constitute the framework of CO_2 based causation in that study. In comparison, CO_2 is shown to relate to both solar activity in **Figure 7b**, and to LEDIV in **Figure 7c**.

4.3. O_3 Fate and Transport in the Hydrosphere

Much like CO_2, ozone is also heavier than air and soluble in water at standard temperature and pressure. But among other important differences, O_3 has a notably different origin than CO_2. In **Figure 9**, the global zonal profiles of the natural log of the mass fraction of ozone are depicted for the first 6 h of January 1979 in **Figure 9a**, and the first 6 h of July 1979 in **Figure 9b**. Ozone appears to originate and concentrate in the middle stratosphere (dark red hues between 30.9 and 38.4 km), upon which it evidently sinks as it circulates in the stratospheric winds. Eventually ozone penetrates the tropopause (signified by the steeper concentration gradient between 11.29 and 23.4 km) towards the surface. In reaching the troposphere, ozone concentrations are significantly depleted, signified clearly by the blue and deeper blue concentration zones, due to interactions with water under less-photolyzing radiation.

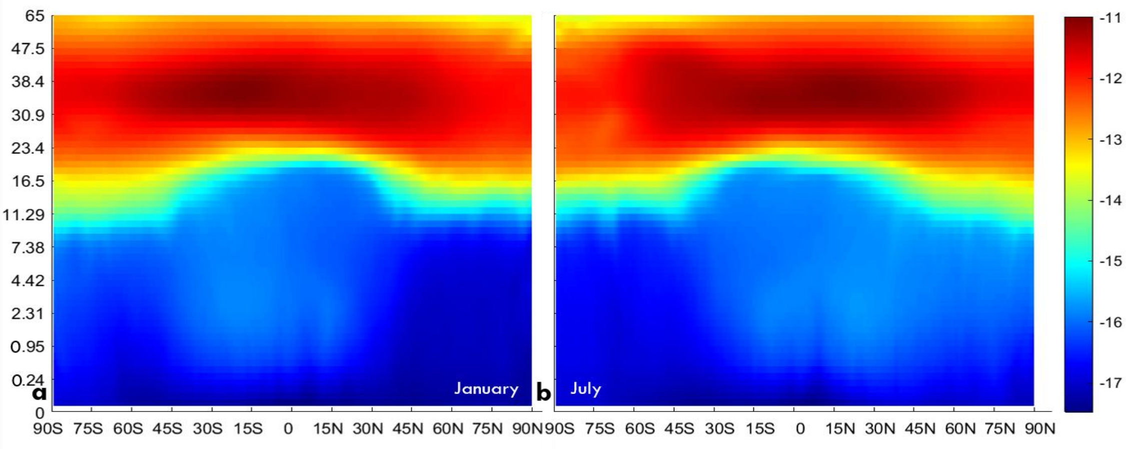

Figure 9. Profiles of global zonally averaged ozone for the first 6 h of January 1979 (**a**), and the first 6 h of July 1979 (**b**).

Note: Color legend in natural log.

Notably, a "plume" is evident for each frame of relatively higher tropospheric ozone (light blue) with a streaking pattern suggestive of ozone "rain". Ozone rain is not widely recognized. Instead, most contemporary literature refers to ozone descent only indirectly via "stratosphere troposphere exchange" (STE) systems[60]. Moreover, interpretations of the ozone "life cycle" such as Chipperfield and Bekki [61], which claim to adopt the WG1AR5 and WG1AR6 climate forcing hierarchy, imply that ozone never significantly leaves any atmospheric level that it is formed in, given their dominant attention to ozone destruction in, and not migration from, the stratosphere. Notably, STE is not described in that study. However, even the WGIAR5 nominally recognizes STE along with other independent studies including Miles et al. [62] and Pound et al. [63]. Pound et al.'s study goes further than most at least regarding our alignment, and identifies ozone deposition onto seawater, which we also subsequently describe.

Perhaps the most important difference from the conventional model is not so much the amount of ozone that descends through the tropopause (which is not controversial), but the rate of stratospheric ozone production. In WG1AR5, Table 8.1 a rate of stratospheric ozone production ~10 times greater than the STE flux is asserted. That is paired with a similar rate of stratospheric ozone destruction. We note initially that both the production and destruction rates are based on models, whereas the STE fluxes are based on observations. We follow up on this subsequently with an alternate accounting and interpretation.

There are related patterns to interpret, again graphically in **Figure 9**. For example, in each frame, the ozone rain in light blue directly underlies the ozone source in dark red. And this system shifts north and the source once each year in line with monsoonal patterns. Clearly ozone is distinctively connected with water in different ways at different elevations. But ozone also seems to share the phenomenon of "overland flow" that water hydrologic runoff exemplifies. As suggested in **Figure 10a**. the small amount of ozone not consumed in tropospheric moisture seems to consistently display gravity-driven overland flow once it reaches any land surface. This is most suggested from the exercise of superposing the ozone surface contours for the year 1992 across the Western US, over that underlying mountainous terrain as the shaded color field. The vector equivalent of ozone concentration is in our representation. It starts with a simple calculation of the 3D gradient of the 3D matrix of pixels representing the ozone concentration. The final step is to invoke the MATLAB streamslice algorithm for the surface layer using those gradient values for 'flows' in the x, y, and z directions.

It is clear from **Figure 10b** that the ozone concentrations align with the potentiometric surface of the landforms. In comparison, the transport of ozone across the oceans is much different. A global adaptation of that figure is shown in **Figure 10b**. The underlying topography is not shown, only the ozone concentration color field. It indicates that surface ozone across the oceans follows the Hadley circulation, first from midlatitudes towards the ITCZ upon which a residuum of surviving ozone is reported—for example by Wang and Fu [64]—to be drawn back up into the ascending limbs of the Hadley Cell (centered over the WEP especially, just as Pacific Ocean surface CO_2 appears to align with, as previously noted).

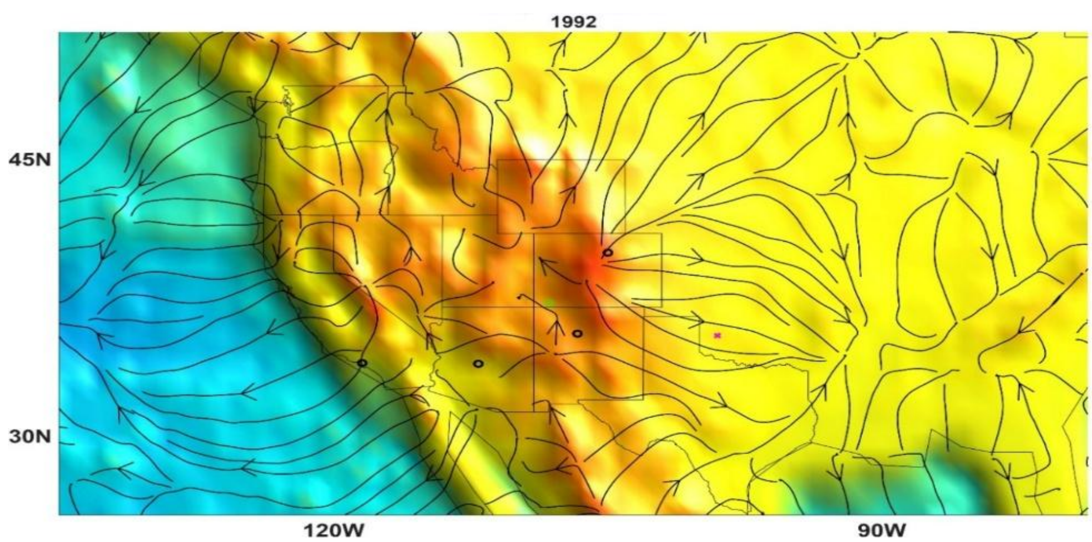

(a)

Figure 10. *Cont.*

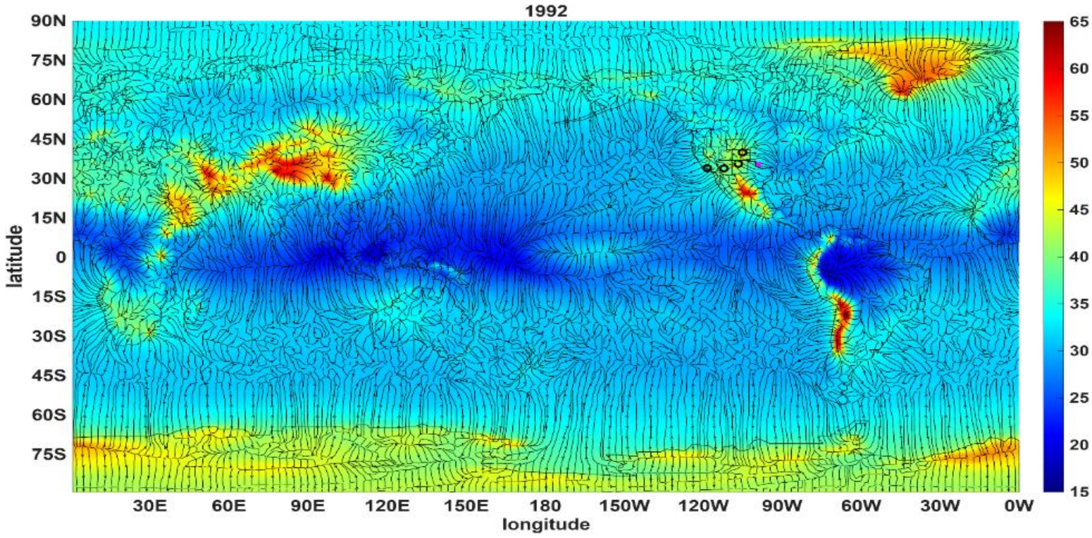

(**b**)

Figure 10. Ozone overland flow conceptual exercise. (**a**) Vector equivalent of ozone concentration (ppbv) for 1992, plotted over a shaded color field map of the topographic (and bathymetric) surface. (**b**) Vector equivalent of ozone concentration (ppbv) for 1992, plotted over a color field map of the same ozone concentration for the same year.

Note: Cities shown as open black circles are clockwise from the center: Denver, Albuquerque, Phoenix and Los Angeles. Green circle for a later predictive exercise. Magenta X not used.

Source: ERAI.

Based upon these collective observations and interpretations, much if not all of the feedstock for ozone may originate from the oxygen that is initially bound in water vapor. This has long been discounted in older chemical hypotheses, along with conflicting concepts of the height of equatorially-convected water penetration into the stratosphere. But as profiled by Dessler[65], the equatorial tropopause can reach up to and above 15 km. Moreover, as observed by Yamamoto et al.[66], a nominal moisture signal can be found as high as 20 km above that footprint, and accordingly, well into the stratosphere. This is the same elevation where ozone is most positively and significantly correlated to moisture in **Figure 11a**. As suggested, further extensive work would be anticipated should these observations and interpretations demonstrate potential for better forecasting of ozone.

Figure 11b profiles the 0-year lagged correlation of zonally averaged ozone with solar activity. Large regions express correlations that are statistically significant, where the absolute value equals or exceeds 0.32 (see **Table A1**). It is relevant to compare this to the ozone phenomenology described in WG1AR5, WG1AR6 and supporting papers since they prioritize ozone climate forcing over solar forcing. Accordingly, our first observation is that both cannot be true. In other words, if solar activity is driving ozone, then the impact of ozone on global temperature cannot exceed the full influence of solar activity on the same parameter. A nearly identical argument was made for CO_2 in previous paragraphs.

Accordingly, much like our CO_2 pathway tracing, it bears emphasis that our concept of ozone origination and transport is at odds with the conceptual model of ozone fate and transport summarized in WG1AR5. For context, that report is based primarily on models that limit calculations to a concept of extreme UV (UV-C, $\lambda < 280$ nm) that causes ozone formation in the stratosphere, pioneered by Chapman in 1930[67]. Chapman (who also speculated on falling ozone) focused on UV-C energy directly photolyzing O_2. Notably UV-C energy at over 150 kcal/mol (627.6 kJ/mol) is sufficient to cleave O_2 bonds ($\Delta H = 493$ kJ/mol). However, water vapor is still present in the middle stratosphere, and only OH bonds need to be broken to free up atomic oxygen from that water vapor. Moreover, the bond dissociation energy for OH of 428 kJ/mol is lower than that for O_2. Accordingly, it appears plausible that water vapor provides a more efficient feedstock for ozone production than molecular oxygen in the stratosphere.

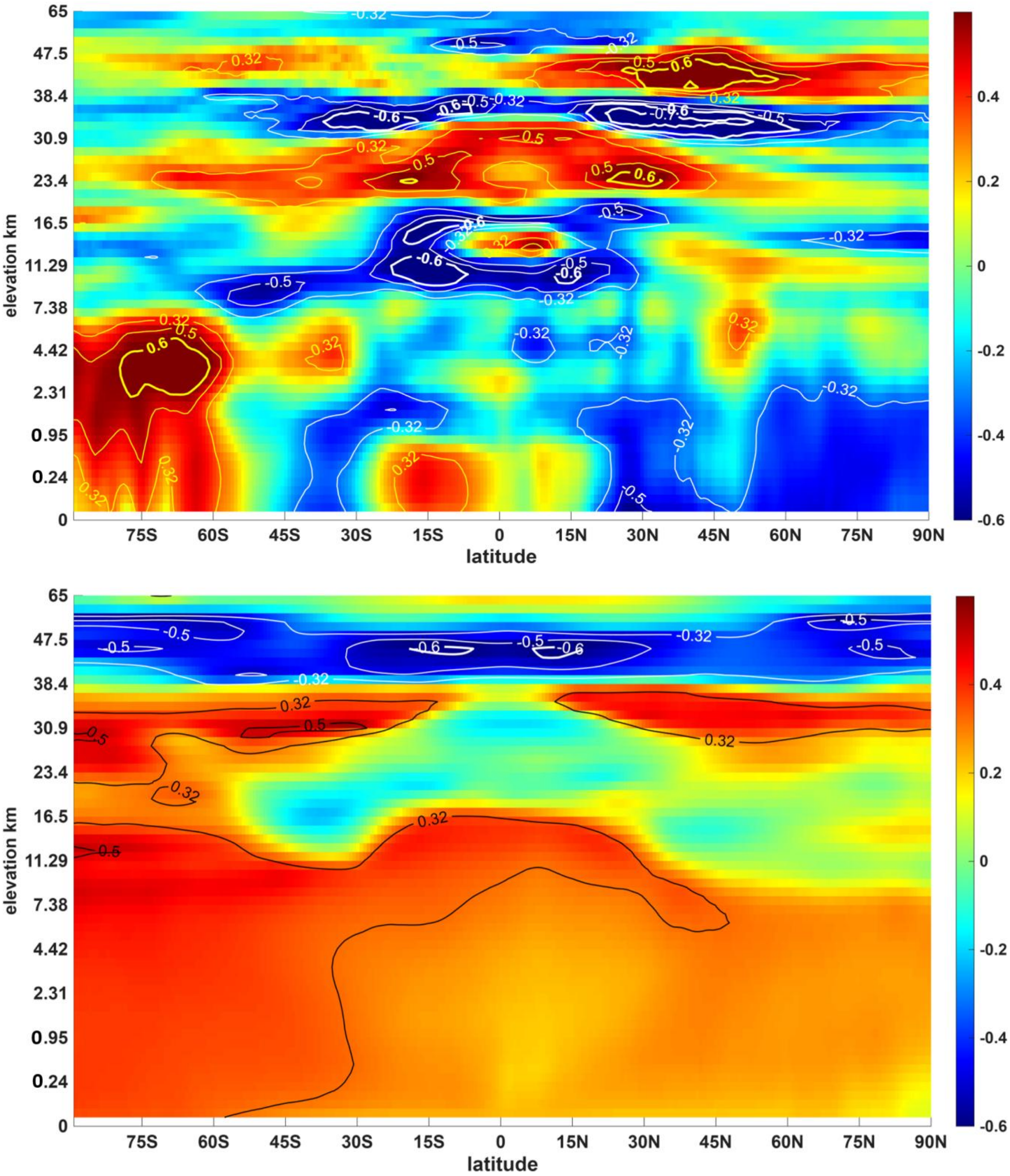

(**a**)

(**b**)

Figure 11. (**a**) Global zonal profile of 0-year lagged correlations of ozone to specific humidity; (**b**) Global zonal profile of 0-year lagged correlations of SSNs to ozone.

Source: ERAI and SILSO.

In comparison, the role of water vapor in WG1AR5, WG1AR6 and supporting documents is limited to a minor source of OH- ions that interact in an intricate and canonical continuum of presumed intermediate species in the two pathways: one of destruction and one of creation of ozone. Moreover, their narrative effectively limits both ends of the ozone lifecycle to the stratosphere. This stands out in contrast to our conceptual model (partially shared by STE studies) that ozone originates in the stratosphere but descends into the troposphere where it expires from moisture contact.

It is also notable that methane is invoked in WG1AR5, WG1AR6 and supporting documents as essentially the sole source of stratospheric water, via a proposed oxidation pathway. And it is interesting in that context that stratospheric methane itself is solely attributed to anthropogenic sources. The chain of equations cited in the WG1AR5, WG1AR6 and supporting literature is extensive but again, they downplay any direct role of Hadley-circulated water that penetrates the tropopause. As noted, water is almost entirely missing from their relevant descriptions of ozone formation and ozone destruction. Moisture is largely superseded by a number of "odd oxygens", identified by only a single oxygen atom in the molecule. Many of these intermediate compounds are identified to be highly reactive, and accordingly they are not commonly observed. Rather they appear to be interpreted more from models than from observations.

We just noted that the extended sets of ozone equations with multiple precursors that support the curation in WG1AR5 and WG1AR6 are based upon models. This is expected to lead to nonphysical results. As described earlier, among other things missing from their conception is ozone "rain" (also termed STE) and other mixed but significant correlations to water profiled in **Figure 11a**. Again, as noted, the WGIAR5 and WG1AR6 products treat stratospheric ozone as largely confined to the stratosphere. In that conceptual model, most of the ozone is produced and destroyed at the same high elevations. Furthermore, the process is implied to alter global temperature due to its destruction by chlorofluorocarbons (CFCs). Moreover, the WG1AR5, WG1AR6 and supporting literature, including Miles et al.[62] primarily attribute surface ozone to derive from photochemical reactions with pollutants at the surface. We note that wherever or however ozone is argued to be produced or destroyed, an anthropogenic factor is invoked as the deciding factor in WG1AR5 and WG1AR6 literature, and the impacts of H_2O and solar activity are not explored.

In contrast, and inspired by **Figure 11a**, we explore the notion that water itself can serve as the primary feedstock for atmospheric ozone production. Trivially, water contains one oxygen atom per molecule. And water is easily dissociated under diverse conditions into an H^+ and OH^- components. Moreover, as noted, OH^- is more easily photolyzed than O_2. And as **Figure 11a** indicates, moisture clearly reaches the ozone creation elevations, and correlates strongly, especially above the equator. We don't expect to sort out the full mysteries of ozone creation, transport and destruction in this exploratory study, but such a notion of water as the primary feedstock for ozone production would add significant value if supported by evidence and if simple to implement.

On that note, although confirmation is well outside of our exploratory scope, it is convenient to initially consider such a mechanism. We begin by comparing the relative quantities of key WG1AR5 stratospheric gases attributed to ozone chemistry, to water vapor content. This is summarized in **Table 2** below.

Table 2. Concentrations (ppm) of selected stratospheric gases at 20 km elevation.

Stratospheric Gas	Approximate Mean Value (ppm)
Oxygen (O_2)	209,500 assumed well-mixed in atm.
Carbon Dioxide (CO_2)	~400 assumed well-mixed in atm.
Stratospheric Ozone (O_3)	~3 (Figure 1 of Anderson et al.[68])
Water Vapor (H_2O)	~3 (Figure 11 of Rosenlof and Reid[69])
Methane (CH_4)	~1.6 (Table 1 of Hsu and Prather[70])

Notably, water vapor is roughly twice as abundant as methane in the stratosphere. This conflicts with the WG1AR5 related reasoning that stratospheric water comes solely from stratospheric methane. Moreover, the proportions of water vapor and ozone are very similar in magnitude. This is particularly evident in the atmospheric concentration profiles in Figure 1 of the Anderson et al.[68]. The stratospheric levels from approximately 20km to 40 km for O_3 and H_2O are shown to be closely aligned. This is suggestive of an (ionic) balance, and since the components are not static, that balance is suggestive of a physical equilibrium. Accordingly, we can initially propose that ozone is primarily created by photolysis of Hadley-upwelled stratospheric water according to this relation:

$$3H_2O + hv \rightarrow O_3 + 3H_2 \tag{3}$$

Where h is Planck's Constant and v is the frequency of the higher energies of UV light found from the tropopause to the mid-mesosphere, where water is also present. Intermediate steps can be anticipated, but as noted for example with the hydroxyl ion, they are not expected to be impediments but rather more catalytic, and therefore facilitative in nature.

A profoundly different expression is widely applied for any encounter of ozone with liquid water wherever photolysis is inconsequential. This holds for much of the surface and all of the night hemisphere.

$$O_3(g) \rightleftharpoons O_3(aq) \tag{4}$$

Between these two governing conditions lies a wide spectrum of possibilities that are in a sense mapped in **Figure 11a**, which again is a global zonal profile of the correlation between the two molecules. In this preliminary approach, many of those intricate patterns are deferred for future studies.

Finally, this work invites additional consideration of prevailing views on photochemical ozone reactions at the land surface, where water is inconsequential. The literature is extensive on topics relating photochemical smog to ozone, including Pollack et al.[71], which chronicles ozone pollution in Los Angeles, US, from 1960 through 2010. That example adopts the widespread model that surface ozone primarily occurs due to photochemical reactions with pollutants including NO_x or other designated precursors[72,73].

In contrast, **Figures 9** and **10a**, support a notion that ozone runoff from high-altitude catchments can account for some if not all of the ozone observed in those previous model-based studies. In any case the accounting of ozone as at least a background component that varies naturally according to STE events is beginning to be more widely recognized in papers such as Bien and Helmig[74].

Our interpretation of ozone rain is consistent with the Bien and Helmig paper, including their observation of greater intensity of natural surface ozone near the summer months, along with their observations that ozone concentrations can be high in areas far removed and "upstream" from major metropolitan areas. To corroborate, examination of **Figure 9** shows that ozone rain is highest across northern mid-latitudes every boreal summer. Moreover, **Figure 10a** shows runoff "trajectories" from high mountains towards both of the featured cities of Los Angeles and Denver. As with numerous other limbs of this paper, much remains to be considered, explored, and tested. But perhaps if and when "ozone rain" and "runoff" gain traction in the surface ozone research community, then more applicable and practical models can be hybridized from existing water runoff models.

4.4. Conceptualization of a "Super Hadley Cell" Based on Coupled Ocean Atmosphere Correlations to Solar Activity

The supporting information to this point is integrated further in the conceptual diagram of **Figure 12**. Much like the preceding data-centric figures, this addresses the circulation and transport of water and energy, along with relevant tracers, through a global profile framework. The schematic is an interpretive diagram based on the featured data that supports numerous concepts and patterns surrounding the main limbs of global hydrospheric circulation. The primary circulation is represented by water (H_2O) via the Hadley Cell, shown in cyan arrows. Through the process of (what we interpret as solar-driven) evaporation, water vapor convects upward from the equatorial surface and spreads to the north and south as it approaches the tropopause. For the most part, water in moist tropical air condenses at the tropopause, releasing significant quantities of latent heat (pink arrow), most strongly over the equatorial footprint, which is ultimately radiated to outer space. Otherwise, wherever H_2O circulates, it gives and takes latent heat along with it. From that perspective, the pink arrows of LEDIV at the top of the equatorial tropopause resemble a global upper-atmospheric "exhaust ring" of the moist static energy not recaptured by water of any state.

Figure 12 is also comparable to Figure 1 of Paltridge[75], which notably equates the entropy of the hydrological cycle with latent heat (LE), and sensible heat (H). Moreover, Paltridge[23] for all practical purposes ("relation 3") surmises that LE is released in association with uppermost levels of cloud growth. The large yellow dotted line terminating in a yellow arrow is intended to represent sensible heat transport from the planetary solid surface (in this case the ocean floor) through the ocean thickness to the surface and on to the atmosphere. This line component is added as a direct consequence of the previous figure sets, which noted strong correlations of ocean pelagic temperature to solar activity in the ensemble of previous images. Above the main box, a single red arrow stands in for the net radiative heat from the top of the atmosphere into outer space. In this case some liberty is taken for the location of the arrow, if only because as noted previously and detailed for **Figures 2** and **6**, the total divergence of energy, TEDIV, reaches maximum "emission" (negative energy flux) at each sub-polar zone.

The energy transfers through the coupled ocean-atmosphere can be expanded upon with the current information. For example, solar activity can now be argued to drive a global convection that spans, effectively (and if only indirectly, given our interpretation of the pelagic zone as the root of convective activity) from the equatorial ocean floor to the top of the atmosphere. Numerous predicates are found in the literature, perhaps most notably by Held and Hou[76]. The original developments in that study adopt a geostrophic version of the Hadley extent which recognizes the divergence of latent heat for "vertically integrated atmospheric energy balance in a steady state". The authors indicated in Equation (26) that the net incoming solar flux S(θ) was equal to the sum of three factors: the heat flux into the ocean F(θ), the outgoing longwave flux measured for the top of the atmosphere L(θ), and the divergence of the atmospheric latent plus sensible heat transport H(θ). The following Equation (5) is adapted from their Equation (26).

$$S(\theta) = F(\theta) + L(\theta) + H(\theta) \quad (5)$$

The Held and Huo study captures some of the primary meridional energy transport across the atmosphere of a radiatively forced spinning hemisphere and dynamically describes a shifting Hadley Cell boundary, along with the associated upper tropospheric jet and a Ferrel Cell. More recent work as noted by Xian et al.[77] also captures eddy and friction effects.

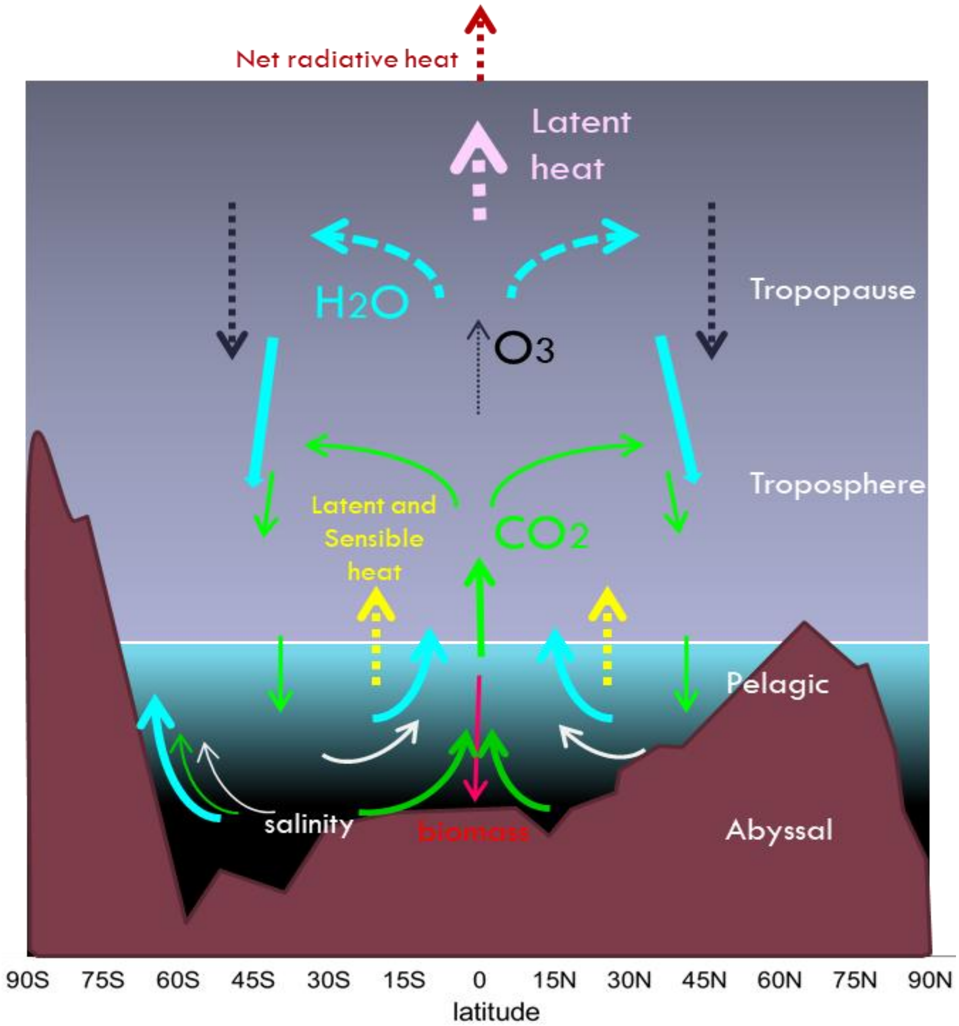

Figure 12. The hydrologic cycle as a solar activity-driven Super Hadley Cell.

A related discussion on solar forcing dynamics, expressed through a damped harmonic oscillator metaphor is proposed in **Appendix C**, which includes a citation to a dynamics paper by Ghil et al.[78]. In addition to purely water and energy-related parameters, the current **Figure 12** also outlines circulations for the four tracers carbon dioxide, salinity, ozone, and biomass. The proposed circulation cycle and/or path for each tracer can be confirmed at least to some extent by collective papers including Xian et al., which do not further address the dynamics of solar forcing relating to the dependent variables of Equation (5). We complement this conceptual model in prior plates in this paper. For example, ozone transport is lightly outlined by the black arrows and those are reflective of the pertinent discussion, including **Figures 9** and **10b**. The salinity limbs in white and the CO_2 limbs in green are again also supported by several previous figures and related discussion.

As mentioned, these are simplifications. One example concerns the Arctic latitudes where no arrows are shown directly. Vortices are noted in the literature in both the atmosphere and in the oceans across those latitudes. These produce additional vertical mixing of moisture and CO_2 but fit within the polar and subpolar cells, which are outside of the Hadley Cell. Finally, the lower vertical red arrow and annotation in **Figure 12** capture the added consideration of biomass sedimentation on the ocean floor. As noted earlier, our conceptual model considers the possibility that this can account for the observed correlations of ocean abyssal temperatures at some locations to solar activity.

Through this construction of data and time series of moist atmospheric, temperature, and related parameters and their correlations with solar activity, a larger more comprehensive model of full-planet convection is derived than the traditional construct. As noted earlier, an expanded Hadley concept was first proposed by Nilsson and Körnich [43], but they did not explore a substantial connection to decadal-scale solar activity. In context, the system profiled in this study incorporates the model of Nilsson and Körnich and expands upon it, to propose a "Super" Hadley Cell that is purely driven by solar activity at almost any secular and geospatial scale and depth from the floor of the ocean to the top of the hydrosphere.

Moreover, regardless of the equatorial pelagic-anchored convection model, or any alternative, our expanded model shows the potential to account for and possibly more skillfully anticipate (predict) global energy, moisture, CO_2, biomass, ozone and salinity transport. From a hydrologic standpoint, moisture is the most important and potentially useful variable to attempt prediction of. Accordingly, a subsequent section features the development of a testable (falsifiable) climate forecast for subsequent evaluation.

4.5. Anomalous Mechanisms of Solar Omission from D&A Studies

As noted in the Introduction, the widely published D&A studies appear to consistently omit solar activity from their detection component. Based on our cited examples, that detection component is limited to studies of whether or not a specific trend may be random. This limitation precludes any CRMA exercises that could potentially recognize connections to solar or other covariates. Accordingly, there is only one place left in the D&A canon to look for solar representation, and that is within the attribution component. However, the attribution component primarily consists of ESMs, which as our Introduction also details, exclude solar dynamics, arguably leading to the documented poor accuracy of many climate simulations.

A broader question arises of how attribution can ever be established by model results alone, even if such models achieve a level of accuracy. Such reliance on models to serve as default evidence ensembles that supersede observations of natural variability, or a related assertion that models can serve as proxies for natural variability, has yet to be authenticated.

Much of this topic is beyond the current scope, but the D&A methodology is at least clear that ESM models are run in two modes: with natural forcing and without. Under the D&A methodology, if selected observations are not skillfully matched by the natural forcing case, then anthropogenic causation is attributed. Again, solar dynamics are missing from both the natural forcing models as well as the anthropogenic forcing models. Accordingly, only models of natural forcing that lack solar dynamics are tested, and not natural variability itself.

In this respect, the D&A studies may bypass sufficient comparisons of any of their models to accepted observations of natural variability. This should be of interest, given that natural forcing has always been the universal default null hypothesis. It is convenient and relevant in this context to cite Rateb et al. [79] in press. That study ran an extensive set of ESM ensembles, under a D&A framework, to compare natural reservoir storage and ultimately showed that the collections of simulations using natural forcings failed to match the observed reservoir variability. This is not surprising because as just noted, the ESM models omit the temporal dynamics of solar activity, and have a long and extensive record of poor accuracy.

Accordingly, it is of further interest to at least roughly trace how solar activity as a causal candidate is separated from ESM model implementations. We interpret that this stems from their procedure of downscaling from global radiation balancing. Perhaps most notably, WG1AR5 Box 8.1 defines radiative forcing by first excluding the impact of water vapor and water condensation. The product appears to advance from there to build models that largely exclude global solar and water dynamics from simulated synoptic impacts. In comparison, our observational study focuses on both solar cycles and water in all states including vapor. And we interpret dry air conditions as well, showing complementary patterns through the TEDIV parameter. Instead of assuming anthropogenic trace gases supersede solar forcing, we work with observed CO_2 and ozone patterns to authenticate (or de-authenticate) our conception of the solar-correlated moisture patterns.

Both approaches of D&A and solar activity would likely benefit from further comparative evaluation. As part of our attention to this topic, the use of balance arguments in WG1AR5 to rule out natural variability is interpreted as a recurring theme. To paraphrase that report, natural forcing agents including CO_2 and O_3 are intrinsically asserted to be in precise equilibrium, and so only anthropogenic factors are invoked to account for any subsequent changes in trends. Following this equilibrium assertion, the global-scaled anthropogenic-specific forcing rankings are accordingly applied (downscaled) in the WG1AR5 products to all local predictive domains. And as noted, this may account for the poor skill of their models.

Again, both approaches cannot be correct. For what it is worth, our approach is based on traceable regressions to authenticated data, whereas the WG1AR5 and WG1AR6 approaches are widely based on numerous intricately-parameterized models. As promoted throughout this study, skillful predictions can play an important role in reaching a balanced evaluation of any candidate approaches, whether the predictions are based on models or on lagged correlations. Accordingly, this paper closes with the contribution of a relevant prediction example, which can be evaluated for skill both now and in the future. In detailing this example, we propose that it would be value-added, before the predictive period is broached too far, for one or more ESMs to be applied by independent researchers towards the same predictive target, for essential comparisons in a few years' time.

5. Applications and Limitations

5.1. Solar Forcing as a Synoptic Predictive Tool

With the cumulative evidence suggesting a solar-driven hydrospheric circulation that takes up to half a decade to complete a circuit, if not somewhat longer, it would be beneficial to consider if there are subsequent synoptic-scaled or more local applications that would improve the skill of climate forecasting. The earlier paper by Wallace [12] also explored this and produced a relatively accurate multiyear forecast for the annual discharge of the Animas River, which was introduced in **Figure 1**. A new forecast of the associated atmospheric parameters, which are naturally required to make streamflows possible, seems plausible under certain cases where the correlations are the strongest and with respect to a few years following a peak or trough in solar activity. It accordingly is timely and convenient for this paper to exercise a multiyear forecast of atmospheric moisture across the same general location as the Animas stream gage, given that solar activity peaked almost two years ago, as also graphed in **Figure 1**.

Figures A3 and **A4** provide the necessary lagged solar correlation information for such a forecast. The figures cover 6 lag cases, from 0 to 5 years, across the US, for 6 moisture-related parameters: surface specific humidity, specific rainwater, geopotential height, surface temperature, fraction of cloud cover, and specific snow water content.

Examination of the cases will corroborate the integrated nature of each variable. In particular, and with close coherence to the previous panels of lagged correlations, the annual surface specific humidity correlations peak across the western US by the third year of lag. That pattern is again evident in the global map featured in **Figure 3a**, which is also for the identical 3-year lag case. Moreover, the same correlation peak lag is evident for the associated other parameters, from specific precipitation to temperature and cloud cover fraction. The directly associated parameters of specific rainwater, fraction of cloud cover and specific snow water content for example all align directly but according to their own characteristics. Furthermore, the parameters of geopotential height and temperature are naturally expected to show peak inverse correlations for the third year of lag, and they do in these examples. This inverse relationship relates primarily to the hypsometric connection between moisture, pressure and temperature widely used in meteorology and hydrology. Notably, as the partial pressure of water vapor increases in the atmosphere, the total pressure drops. This additionally impacts temperature (T) via the Ideal Gas Law.

With the timing of the most recent solar activity peak in mind, we elected to follow the example of **Figure 1** for the

Animas River, and make an equivalently scaled three-year advance projection of the five-year trailing average (5yta) of the specific rainwater content for a location overlying the Animas watershed footprint. Previous work of Wallace[12] explored a range of lags and multiyear averages for the Animas location, and found that a 5-year average with a 3-year lag led to the strongest correlations and *p*-values, according to the paper's adopted frequentist framework. Accordingly, we start with this configuration for the projection exercise. Our location selection is shown in **Figure A5**. The lagged correlation map shows both the older Animas River location as an open black circle just west of an open blue circle with a green center. That location is also green from the correlation contour manually assigned for a correlation of 0.8, and it is upstream from the Animas location. Areas of such high correlation are not common, but the highest correlated areas are expected to yield the most skillful forecasts. The correlations of nominal statistical significance are shown within the dotted black outlines of R = 0.6.

The outcome is featured in the final **Figure 13**, which indicates a relatively close alignment of the hindcast SP (blue open circles) to the observational record (solid magenta curve) in that location. **Figure A7** documents the initial development through a scatterplot of the solar activity compared to the rainfall activity. The linear regression fit is the basis for the equation used to develop the cyan time series in **Figure 13**. Notably, and accounting for the moving five-year average, the forecast is for an increase in specific rainwater content across the target area (northwestern New Mexico and southwestern Colorado) by 2028.

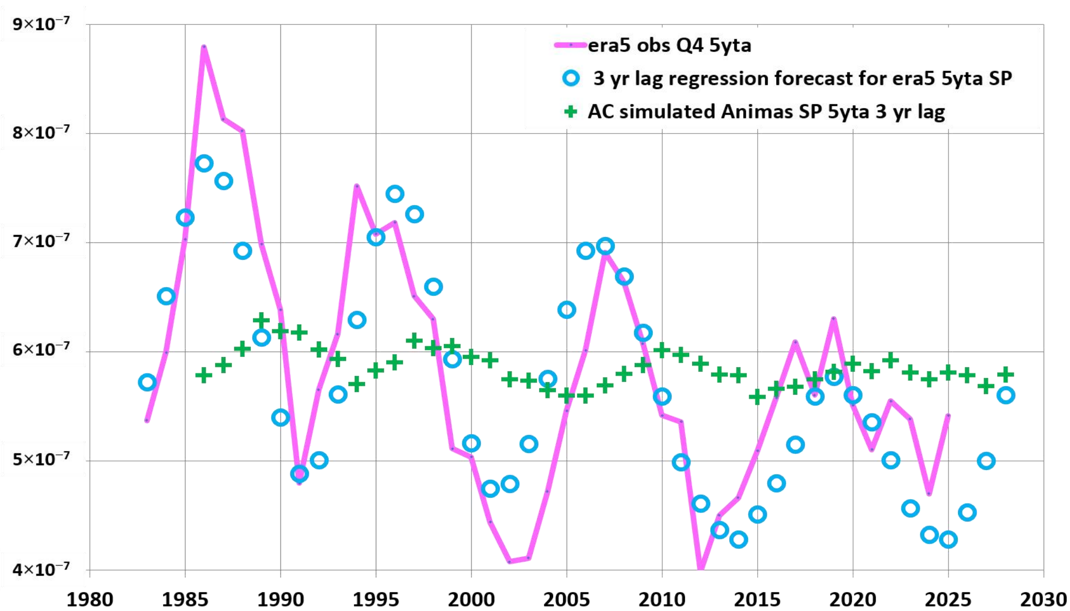

Figure 13. 3-year lagged solar activity (SSN) based regression hindcast and forecast for specific rainwater content near the USGS Animas River gauge in northwestern New Mexico.

We have proposed earlier that nothing is better than a skillful and meaningful (not trivial) forecast at validating a causal candidate to any extent. Yet it is common to attempt to approach a better understanding of the causes of a given time series through cross regressions, before waiting for a forecast to play out, for further judgement of prognostic skill. Numerous accepted conventions for evaluating formal correlation series and maps are possible, such as the Nash-Sutcliffe Efficiency test (NSE) which is widely used as a "calibration summary statistic" in the US Army Corps of Engineers (ACE) HEC-HMS flood modeling and forecasting applications (see https://www.hec.usace.army.mil/confluence/hmsdocs/hmstrm/calibration/calibration-summary-statistics). The associated NSE index is accordingly for this exercise equal to 0.66 (detailed in **Table A4**). Any NSE value, from 0 to 1 signifies that the projection is better than a simple average-based (in our case, climatological) projection, with 1 signifying a perfect prediction.

Other approaches often follow templates for screening out autocorrelation, thereby accounting for persistence and for quantifying skill. Such examples can be found for example in Guemas et al.[80], Trenberth[81] and Tuel and Martius[82], along with many other resources.

With those considerations in mind, we elected to follow two paths to substantiate the forecasted low impact of AC. We accomplished this first by following the published example in Wallace 2019, which directly compares AC-based hindcasts to solar-based ones as shown by **Figure 1**, and also now included in **Figure 13**. Notably the AC-based regression hindcast in green crosses is much less aligned (correlated) to the magenta observational record than the solar activity regression hindcast. **Figure A8** is additionally provided to more clearly quantify the relative errors of the two hindcasts, following the same example of **Figure 1b**. Again, the AC skill is shown to be relatively poor in comparison to the solar-based projection skill, and the extremes of droughts and fluvials are again better anticipated by the solar-based projections both future and retrospective.

In addition, we applied the widely used technique of calculating and mapping the autocorrelation of the regression residuals (ACOR) in **Figure A6**. Notably and as expected for the solar "hypothesis", the ACOR is low where the solar activity correlation is high. We also conducted a Granger Causality calculation on the same SSN and SP time series featured in **Figure 9**. Although the word "causality" is associated with the test name, this is not interpreted literally. **Figure A9** captures the details of the calculation as it applied to the predictive power of the independent SSN variable. With a p-value = 1.17×10^{-5}, solar activity (via the SSNs) is interpreted to provide significant predictive power for the atmospheric moisture variable SP within this high cross-correlation limited region.

Following up on the Discussion content, this study has closed with an exercise to test the apparent predictive power of a lagged solar approach. In a few years, the accuracy or inaccuracy of the featured forecast will further reflect on the validity of that potential. That will also serve as a de facto out-of-sample validation (OSV).

In any case, we also revisited a past skillful solar-based hydrology forecast for the same locale[12]. The skill of that prediction, along with the extensive profiles, correlations, and interpretations of this study also challenge the claim of low solar sensitivity framed in the hierarchy of climate forcing by Gray et al.[1], and adopted by the majority of contemporary GCMs along with WG1AR5.

A reason for some of the gap may be that the positive and negative solar correlations are roughly equal in magnitude and therefore tend to cancel each other out when averaged over the entire planet. That would be interesting to quantify further, but the fact remains that GCMs apply considerable effort to model the full planetary footprint in some detail, and so these correlation patterns, along with the latent heat distributions featured here should be evident in any skillful GCM result. Finally, the ACOR tests for greenhouse gas climate-forcing interpretations, along with the other numerous candidates appear to remain relatively unexplored.

5.2. Limitations

While lagged solar correlations offer the potential to explain many aspects of sub-decadal climate dynamics, they aren't anticipated to explain everything. For example, the bulk of most related maps in this study suggest that approximately half of our atmosphere and ocean volumes are relatively uncorrelated to solar activity at these scales and lags. This might be attributable to eddy diffusion, but for this initial exploration, we have not attempted any exercises or cited any further work to develop that concept. Even for the cases and regions of highest lag-correlation, much dynamic uncertainty remains depending on the general and/or specific application. That is among many reasons why if better climate predictivity remains of interest, we ultimately favor the development of sustained empirical, transparent track-records of forecast accuracy performance that accompany related papers on causality and trend detection.

We also recognize the relatively early stage of reanalysis products (~50 years). Much like many, we naturally expect further solar-considering investigations of existing data as well as the accrual of additional years and decades of relevant important data. Given our expectation that subsequent investigations will routinely digest increased resolution in geospatio-temporal information, and an equally important anticipation for improved modeling that practices parsimony in parameterizations, we expect these will lead to additional independent and value-added interpretations which might improve the range and fidelity of subsequent multi-year climate forecasts.

For example, apart from **Figure 3d–f**, our study has not focused on trends of the parameters. That was largely excluded from this exploratory study which instead focused on lagged solar correlations of the parameters. Yet much like many conventional trend–detection techniques, we applied linear regression for all of our correlation exercises as well as those few trends that we did calculate. From those results, we found substantial support because those mapped trends aligned with solar correlations. And the lagged cross-correlation exercises we conducted were further substantiated by quantification of serial (auto) correlation. This is a consideration which is described in many trend-detection studies as well, although not in the previously cited studies by Didovets et al.[10] or Wang et al.[11].

Arguably, our exercises would be an important consideration for subsequent climate trend studies, if only because, where most statistically significant, solar activity correlations provide additional predictive information, beyond what the null hypothesis of random natural variability would project. In comparison, D&A trend investigations widely adopt the Mann-Kendall test, which assumes that random conditions are to be tested against. We accordingly propose that future D&A studies would benefit by instead beginning with the consideration of a much less random solar influence. Then like any null hypothesis, if solar influence can be subsequently ruled out, then parametric or non-parametric trend analysis methods, including the Mann-Kendall test, could at least advance having defined and/or mapped the limits of the statistically significant areas.

Contemporary researchers are likely to carry on in any case with trend and other techniques that they interpret to be merited, from non-linearity to examinations for "false detection rates" (FDR). We nonetheless recommend that where relevant, those exercises include some simple solar correlation exercises along the lines that we conducted, to ensure that the solar hypothesis is not pre-emptively discarded. Avoiding the consideration of the "solar hypothesis" might be equivalent in practical terms to a false rejection rate, which as noted throughout our study is analogous to solar activity's current position at the bottom of the WG1AR5 and WG1AR6 climate-forcing hierarchy.

Finally, we note limitations in the temporal spans of applicability. Our demonstrations of prediction have focused on sub-decadal time frames. Given that each solar cycle follows a roughly 11-year span, the method outlined here does not allow for predictions beyond a certain fraction of that limit. Furthermore, predictions for smaller scales of time than the annual time frame are also expected to be challenging. For example, the quantitative prediction of a variable such as atmospheric moisture or temperature for a given month, even within a high solar-correlation areal footprint, might be difficult if not impossible for many cases. That remains to be tested. Some non-quantitative, more categorical monthly or seasonal forecasts do seem worthy of exploration from a solar causation perspective. In that respect, they might be similar in methodology to common ENSO-based seasonal forecasts. And in that respect, it is already noted in this and other papers that ENSO itself has a solar correlation aspect which is not widely recognized.

6. Conclusions

Through examinations of satellite reanalysis and other data, we found that the temporal variations of major ocean and atmospheric circulation parameters, including salinity, temperature, and atmospheric moisture, are lag-correlated with solar activity, forming dynamic patterns across the Earth's surface. Positive and negative correlation domains that emerge and decline over periods of several years were interpreted to outline coupled ocean-atmospheric circulation manifolds with opposing responses to solar activity. These domains were found to be evident in binary contrasts from pole to equator to pole, and from the ocean floor to the surface and on to the top of the atmosphere. The correlation waves emerge at 0 years of lag and typically reach peak intensity by the third year. Those signatures decay within a few additional years. Ocean correlations were found to be notably stronger and more persistent than atmospheric ones.

These opposing correlation waves are separated by a distinct chevron (sawtooth) meridional boundary that roughly aligns with 180° E longitude. We have cited studies by Xiao et al.[32], and Huo et al.[33], to term this an extended meridional solar correlation dipole. This is argued to result from latent heat exchange impacts at the ocean surface and the tropopause due in part to the alignment of those reversals with those signatures. Data and lagged correlation analyses also suggest that a portion of the radiation from solar activity reaches the equatorial band of the pelagic zone and stimulates convection, potentially influencing surface evaporation and supporting a broader meridional overturning along with several distinct and independent oceanic convective regimes.

We accordingly developed a conceptual, integrated profile of hydrospheric global circulation limbs which cover the limits for water and air. We term this system a Super Hadley Cell and relate it closely to associated dynamics and global patterns of latent heat exchange. Because of the lagged solar correlations in the context of the conceptual model, the predictability of decadal climate and hydroclimate changes was discussed and analyzed. This included a sample quantitative forecast of moistening across a target area of the Southern Rocky Mountains over the next three years, which would represent a significant departure from the current warm-and-dry trend. Among other skill metrics we applied, Nash-Sutcliffe Efficiency (NSE) was calculated to be 0.66 for the hindcast exercise, which is higher than a climatological-mean baseline.

Important disparities have been identified between high solar correlations and their relative absence in the climate trend-detection and attribution (D&A) literature. This also highlights the dependence of global earth systems models (ESMs) on parameterizations. Our work concludes in part with an interpretation that those parameterizations do not facilitate an accurate and dynamic representation of the relative importance of solar activity on annual- to decadal-scale synoptic climate.

Also, in examining the mechanisms of climate forcing modeling most clearly summarized in WG1AR5 and WG1AR6 that relate to and/or conflict with solar correlation patterns, several interpretations have been discussed, which still require mechanistic verification:

- GCM studies developed a climate forcing hierarchy based on global radiative interpretations, and then applied these locally (i.e., synoptically or finer in scale). Through this global filter, parameters like solar activity, which are documented in our study to exert more local impact appear to have been screened out.
- GCMs subsequently rely heavily on parameterized forcings of significant magnitude that are primarily attributed to both CO_2 and ozone among other candidates.
- The elevated attributed climate forcings of CO_2 and ozone over solar activity have not been reconciled with observational data profiled in this study. Notably, as featured in the Discussion section, both CO_2 and ozone are significantly lag-correlated to solar activity, and their mapping shows further alignment with the aforementioned Super Hadley Cell. These correlations and alignments pose a number of challenges to the interpretations in WG1AR5 and WG1AR6. For example, we have argued that if the two gases are lag-correlated to solar activity, then their position in any climate-forcing hierarchy cannot logically supersede the position of solar activity itself.

With regard to the inconsistencies in those ESM-related products, it follows that an increase in attention to transparent authentications of predictive skill and more should in fact be applied equally to both solar activity and other attribution studies of climate forcing and causality. Moreover, this could be applied equally to both modeling and to trend analyses, perhaps leading to hybrids that improve the state of prediction and diagnostics.

Our broad notion of a Super Hadley Cell was shown to be consistent with the extensive atmospheric and ocean data as well as our proposed mechanism of circulations and latent heat exchange. But the solar-driven Super Hadley Cell remains a hypothesis, requiring further independent testing. The associated solar activity-based forecasting and hindcasting exercises and results demonstrated predictive skill, but do not in their own right establish confirmation of the hypothesis. Further independent work on all lines of discussion and evidence is anticipated and merited, before this hypothesis can significantly advance. The same need for additional confirmation and clarification is expected for any climate studies which currently disregard or diminish the role of solar activity. Perhaps as a result of this study, solar activity will be more explicitly and dynamically accounted for in relevant future D&A and associated ESM studies.

With that in mind, although many areas of statistically significant solar correlation have been mapped here, the significance may still not be great enough to routinely translate into skillful forecasting. The examples shown were limited to 5-year trailing averages because solar correlations are higher for that product than for series using annual averages. Moreover, these 5yta forecasts were localized to a region of the US with the highest such correlation, approximately R = 0.8, which is much higher than in most regions of the planet for any variable considered at any lag. Accordingly, effective application remains to be developed if ever possible, for shorter time periods including annual and monthly products, applying solar activity series in the proper context and likely often with other covariates where merited.

Author Contributions

All authors contributed to the study conception and design, along with the final form and content. Material preparation, data collection and much of the analyses were conducted by M.G.W. Causality and related analyses, along with complementary hydrological aspects were conducted by B.F. Geochemical and hydrological coupling aspects of the manifold of related topics were led by Y.W. All authors have read and agreed to the published version of the manuscript.

Funding

The authors declare that no funds, grants, or other support were received supporting the development of this work.

Institutional Review Board Statement

No animals or human subjects were involved in this investigation. Accordingly, this work did not require an associated institutional review.

Informed Consent Statement

No animals or human volunteer subjects were involved in this investigation. Accordingly, no informed consent documentation was required or developed.

Data Availability Statement

All primary data are accessible via the links provided in **Appendix A**. Any additional minor datasets for specific time series are available upon reasonable request to the corresponding author.

Conflicts of Interest

The authors declare that no direct financial interests apply to the publication of this work. M.G.W. runs a small business in hydrosciences and considers and informally posts about solar forcing routinely. He is always careful to provide context and to distinguish from peer-reviewed content.

AI Use Statement

No AI tools were used for data analysis, interpretation, or generation of scientific content.

Appendix A. Data Resources and Methods

Our products are derived through literature reviews and from additional data sources which are further developed into geospatial time series. We apply linear and statistical methods, using MATLAB and Microsoft Excel to the data sets in various trials and contexts of relevance to the focus of the paper. **Table A1** is included for convenient interpretation of the numerous correlation contour overlays and color fields. And **Table A2** provides references to all datasets and methods.

Two ECMWF (European Center for Medium Range Weather Forecasts) datasets are primarily relied upon in this study, the operational version (ERA5), the interim set (ERAI) and the University of California at Riverside (UCAR)[18]. Each variation develops records of weather and atmospheric data into a uniform, continuous, and relatively high resolution geospatiotemporal coverage of our planet's atmospheric condition. Many variables and derivative variables have been tabulated, including winds, temperatures, pressures, divergences of energy, and atmospheric moisture. Moreover, ERAI is noted to be the first 4Dvar scheme for reanalysis[19].

This study, along with the previous work by Wallace[12] also relied upon the SILSO Belgium source for solar radiance proxy data as sunspot numbers (SSNs). Both studies include comparisons of annual and trailing five-year averages (5yta) of parameters from the UCAR resource, which is an integration of the full atmosphere from the parent ERAI database[18]. The UCAR set also extrapolated the ERAI data's upper limit, from 65 km altitude to 100 km. Our examination of the data also continues to utilize the UCAR source. Due to their geostrophic reduction of the atmosphere to a single integrated layer over 36 years, file sizes are relatively small, even as their information density and value remain high. Accordingly, with the limitations in mind, the monthly UCAR geostrophic datasets offer convenient analysis of globally spanning circulations.

This study more fully addresses vertical profiles, along with layer and surface maps, of parameters and their trends. Most are explored with the ERA5 series.

Methods include data graphing with both Microsoft Excel 2007 and a commercially licensed version R02023a of Matlab.

Matlab was additionally used for correlation calculations and mapping using the “correl” function. All trends were calculated for the linear fit setting only.

Stream slices developed through Matlab are sensitive to the assigned density in the final entry of the MATLAB command. We note that our use of the density assignment at the end of the command must be assigned for reproducibility.

```
meanSlab=streamslice(MeanSlabZon,MeanSlabMert,MeanSlabVert,2,[],[],3);%for average of all years
%meanSlab=streamslice(kZonAv,kMertAv, kVertAv,2,[],[],3);%for a year
set(meanSlab, ‘Color’, ‘black’); set(meanSlab, ‘LineWidth’, 5);
```

Color fields for most graphics are directly mapped to underlying data with a filter using the “caxis” command in Matlab. In addition, typically the Matlab “colormap” commands for “Jet”, “Parula”, and HSV are used. Apart from the few uses of HSV, a convention is followed throughout the paper that the deepest blue represents the greatest negative or absolute limit (depending on context) and the deepest red (or yellow in the Parula case) represents the greatest positive or absolute limit, depending again on context. For the trend maps and profiles, a white contour line representing the zerotrend boundary is included.

Frequently, we have also overlaid contours and/or vector and/or landform variables onto trend and/or correlation figures. Some contours are provided for context of another subject, but often they are intended to convey a quick sense of the statistical significance variation across a correlation map or profile of any kind. In those cases, we often start with a white zero correlation line, which is obviously the least statistically significant, but which defines a rough and robust boundary between positive and negative correlations. We then factor N, the number of common time series entries for the parameters with R, the Pearson linear correlation coefficient, to define the contour that corresponds to the value $p \leq 0.05$, which defines the widely used 95% confidence boundary. At times we note cases where $p \leq 0.01$ which defines the 99% confidence boundary.

Table A1. *p*-value guides and related parameters for correlation contours.

Resource	N	Cell Size (Years)	Lag Size (Years)	R for *p*-Value = 0.05	
UCAR, MPI	36	1	1–4	0.39	The *p*-value is 0.018704. The result is significant at $p < 0.05$.
ERAI	40	1	1–4	0.32	The *p*-value is 0.044119. The result is significant at $p < 0.05$.
ECCO	26	1	1–4	0.39	The *p*-value is 0.048884. The result is significant at $p < 0.05$.
ERA5	46	1	1–4	0.3	The *p*-value is 0.042803. The result is significant at $p < 0.05$.
ERA5 for 5yta case	43	5	3	0.31	The *p*-value is 0.043068. The result is significant at $p < 0.05$.

Sometimes broad areas of a solid color are evident in the correlation figures. These usually develop when areas express even higher correlations than the assigned color range mapped to from −0.6 to +0.6. And that develops from applying one color field scheme limit to all lag cases from zero to 4 or 6 years. Accordingly additional contour lines are typically added to fill out that information.

When figures are not explicitly labeled, the convention is adopted that the uppermost figure or the upper left figure is considered to be ‘a’. From there, the labeling advances to ‘b’, ‘c’, etc., either top down, or clockwise, or at times from left to right, depending upon the layout and number of images.

Table A2. Data and methods resources.

Data ID	Acroynm	Link
Sunspot numbers SSNs	SILSO	https://www.sidc.be/silso/home
Satellite atmospheric reanalysis data and planetary topography	ERAI and ERA5	https://www.ecmwf.int/en/forecasts/datasets/reanalysis-datasets/era-interim https://www.ecmwf.int/en/forecasts/dataset/ecmwf-reanalysis-v5

Table A2. *Cont.*

Data ID	Acroynm	Link
Satellite atmospheric reanalysis data full atm integration	UCAR	Vertically Integrated Mass, Moisture, Heat, and Energy Budget Products [18] Derived from the NCEP/NCAR Reanalysis March 2003 Climate Analysis Section, CGD, NCAR Contact: David Stepaniak; davestep@ucar.edu Downloaded on 3-10-2016 from http://www.cgd.ucar.edu/cas/catalog/newbudgets/index.html#ERBEFs– files ERAI.Z.1979–2014.nc, ERAI.LEDIV.1979–2014.nc.ERAI_TEDIV.1979-2014, ERAI.U.1979-2014, and ERAI.V.1979-2014
Ocean zonal, meridional and vertical velocities	PODAAC https://podaac.jpl.nasa.gov/ECCO?tab=mission-objectives&sections=about%2Bdata	ECCO Consortium, Fukumori, I., Wang, O., Fenty, I., Forget, G., Heimbach, P., & Ponte, R. M. 2021. Synopsis of the ECCO Central Production Global Ocean and Sea-Ice State Estimate (Version 4 Release 4), Zenodo. https://doi.org/10.5281/zenodo.3765928 [20] ECCO Ocean Velocity-Monthly Mean 0.5 Degree (Version 4 Release 4) (ECCO_L4_OCEAN_VEL_05DEG_MONTHLY_V4R4)
Animas River discharge time series	USGS	US Geologic Survey Water Data for the Nation https://waterdata.usgs.gov/
Ocean – Atmosphere CO_2 exchange	MPI	Landschützer, Peter; Bushinsky, Seth; Gray, Alison R. (2019). A combined globally mapped CO_2 flux estimate based on the Surface Ocean CO_2 Atlas Database (SOCAT) and Southern Ocean Carbon and Climate Observations and Modeling (SOCCOM) biogeochemistry floats from 1982 to 2017 (NCEI Accession 0191304). Version 1.1. NOAA National Centers for Environmental Information [21]. Dataset. https://www.ncei.noaa.gov/access/metadata/landing-page/bin/iso?id=gov.noaa.nodc:0191304 [2019-07-17].
Methods		Matlab vs. R2023a Update 4 (9.14.0.2306882) was used for most data graphics other than time series curves (Microsoft Excel) and the conceptual illustrations. Matlab was also used for all correlation exercises featured in the study. R (Studio Version 2023.12.1+402) was used for Granger tests.

Spatial and Temporal Scales of Data

Although all resources offered a common monthly data resolution, each resource utilized different spatial scales of data. These are outlined below and summarized in **Table A3**.

Temporal Scales

Our time scales of interest primarily range from years to sub-decades for both the variable sets and the time lags used in the correlation exercises. Although we have focused on time series with a yearly increment, we largely develop those from data that had a monthly resolution.

Spatial Scales

Our spatial scales vary, depending upon the source data. For example, the ERAI datasets are 4Dvar, with 60 layers in the vertical reaching from the surface to the stratopause. There are 480 divisions of longitude and 241 divisions of latitude. We downloaded monthly resolutions of the data of interest for totals of up to 480 time-steps (40 years). The subsequent ERA5 datasets utilize 14,440 divisions of longitude and 720 divisions of latitude.

These scales in time and space and related exercises are comparable with much of Wallace's previous study in 2019 [12], but encompass more refined temporal scaling along with greater dimensionality as well as attention to the meridional perspective of trends in higher latitude variables, reaching to each pole. Again, for these refinements, our study routinely limits the temporal increments to years, thereby screening out most seasonal topics. Any significant seasonal trend would be evident, and accordingly, already implicitly captured, in an annual scaled trend.

Table A3. Spatial and Temporal scales for data resources.

Resource	Temporal Resolutions and Total Length in Years, Beg and End Years	Pixel Resolution (Zonal by Meridional by Elevation) for Cases Used
UCAR	monthly, yearly 36 years, 1979–2014	512 × 256 × 1
MPI	monthly, yearly 36 years, 1982–2017	720 × 360 × 1
ERAI	monthly, yearly	

Table A3. *Cont.*

Resource	Temporal Resolutions and Total Length in Years, Beg and End Years	Pixel Resolution (Zonal by Meridional by Elevation) for Cases Used
40 years, 1979–2018	480 × 241 × 60	
ECCO	monthly, yearly 26 years, 1992–2017	720 × 360 × 50
ERA5	monthly, yearly 47 years, 1979–2025	1440 × 721 × 1
ERA5 for 5yta case	monthly, 5-year average 47 years, 1979–2025	1440 × 721 × 1

Appendix B. Additional Lagged Solar Correlation Maps and Other Content for Featured Variables

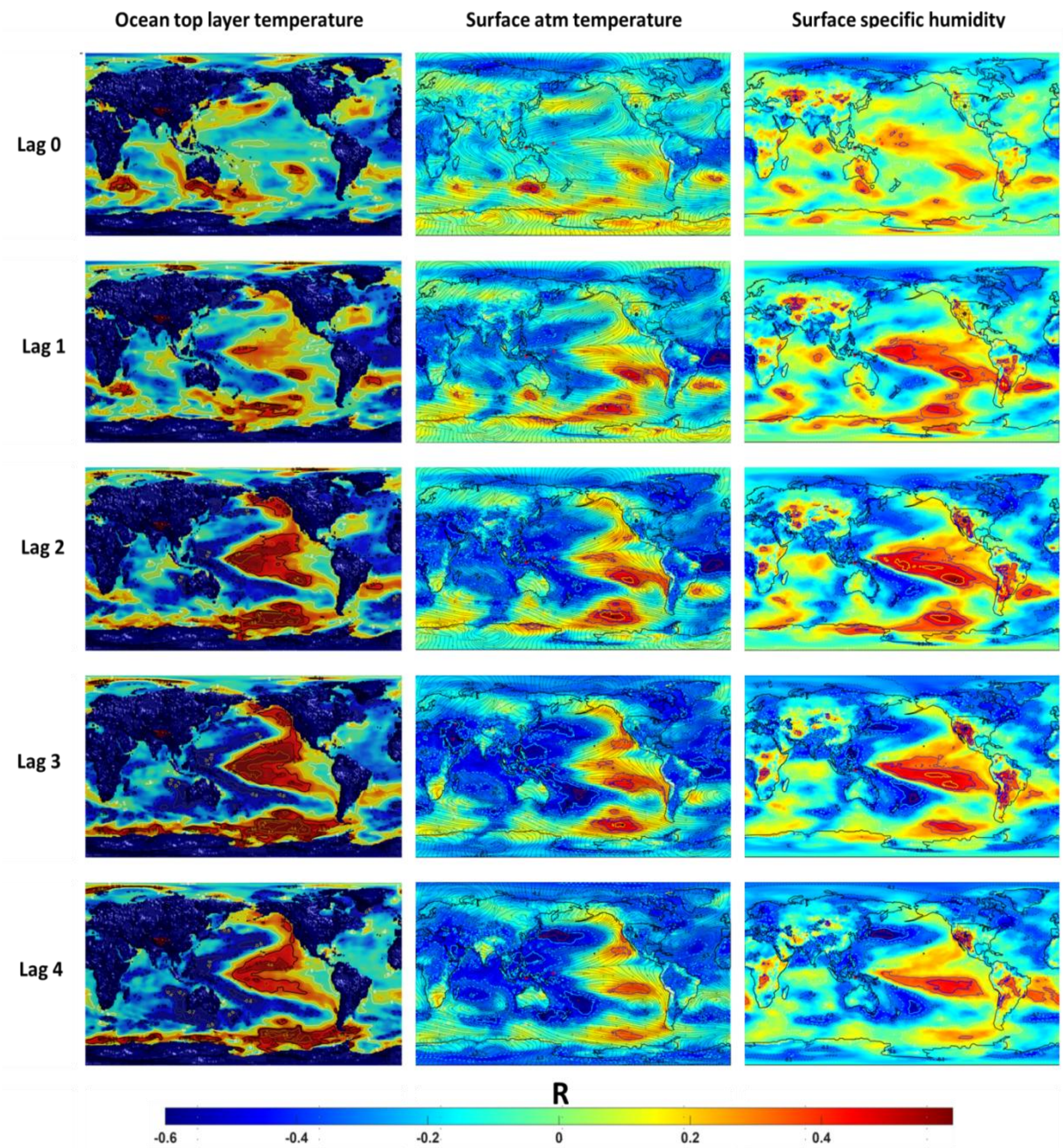

Figure A1. Lags 0 through 4 years (rows) for the correlation of SSNs to the temperature at the uppermost layer of the ocean (ECCO layer 50) (left column), to the surface temperature of the atmosphere (middle column) and to the specific humidity at the surface (right column).

Source: Developed from sources ERA5, ECCO, and SILSO.

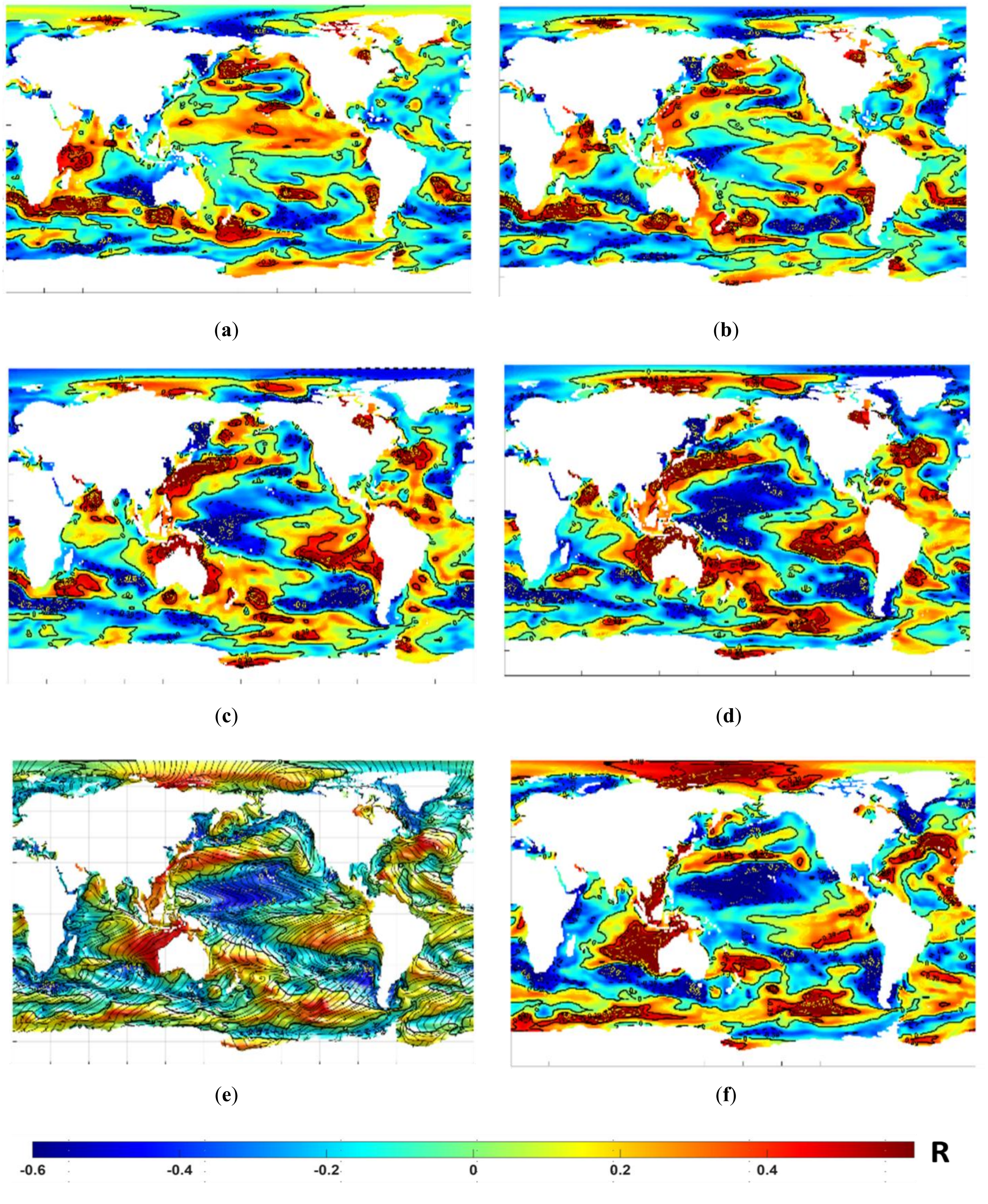

Figure A2. Lagged correlation of global ocean surface salinity to the sunspot number series. (**a**) Lag 0 year. (**b**) Lag 1 year. (**c**) Lag 2 years. (**d**) Lag 3 years. (**e**) Lag 5 years. (**f**) Lag 6 years.

Source: ECCO and SILSO.

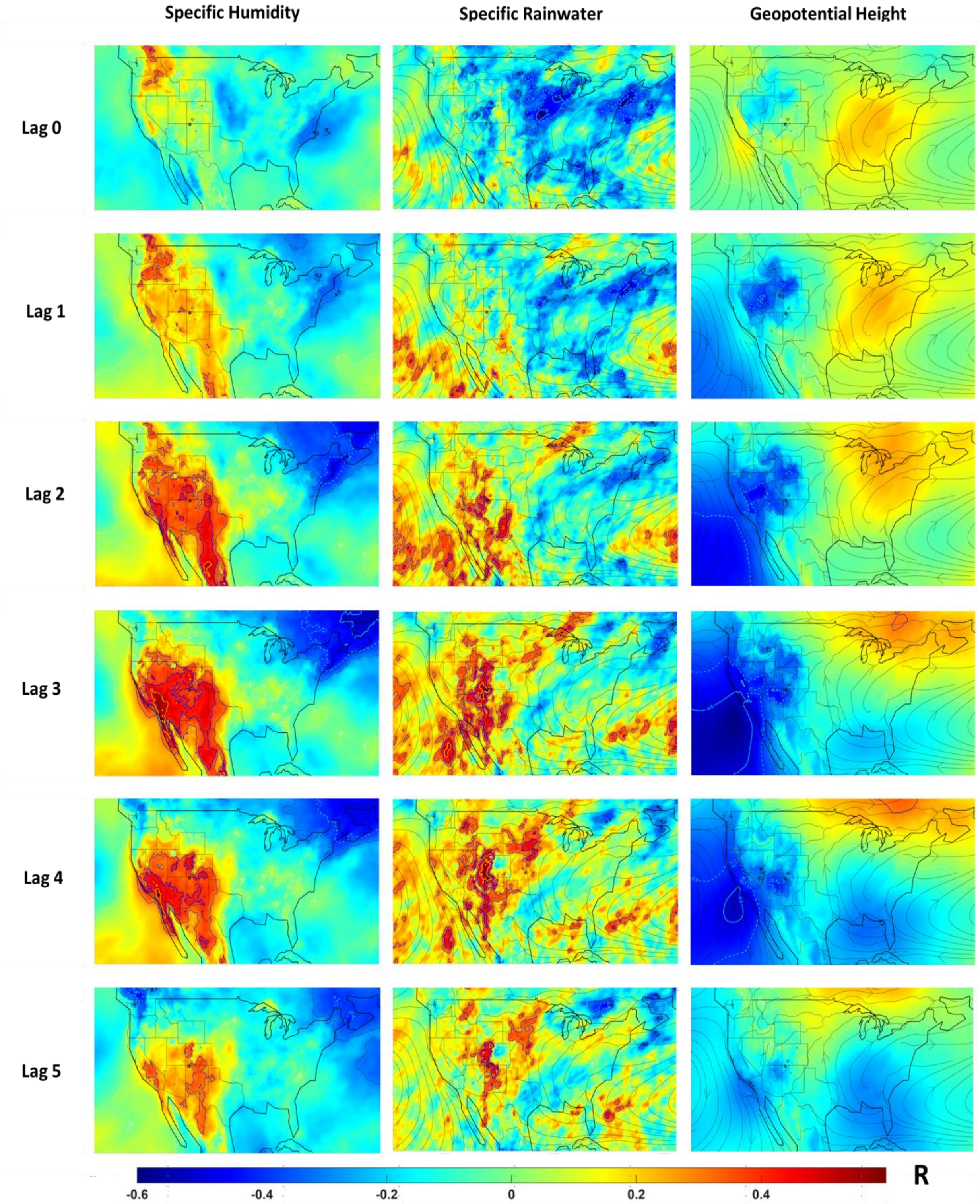

Figure A3. Lagged correlations of surface specific humidity (left column), specific rainwater (center column), and geopotential height (right column) across the US to solar activity over 6 cases of lag, from zero to five years.

Source: SILSO and ERA5.

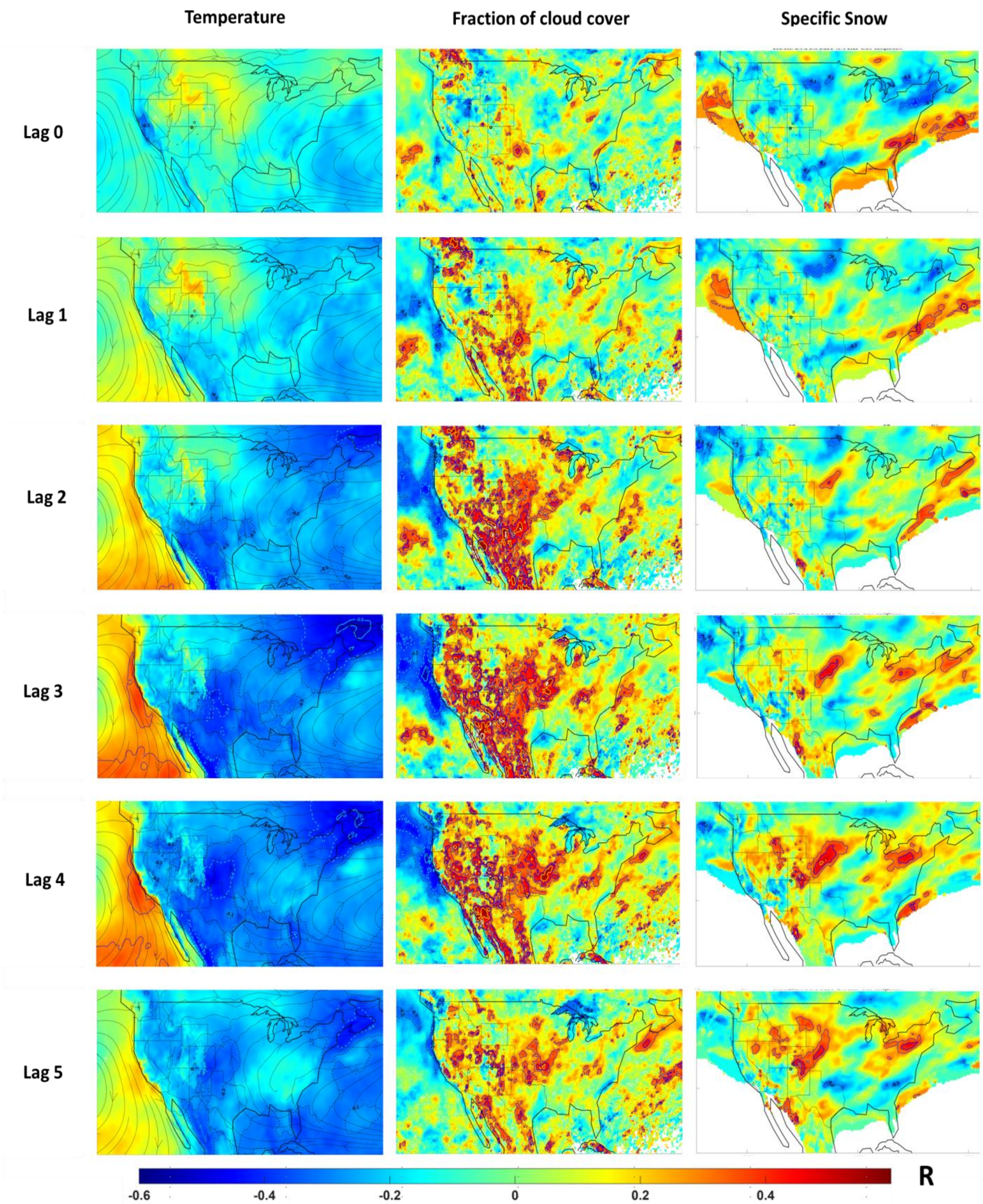

Figure A4. Lagged correlations of surface temperature (left column), fraction of cloud cover (center column), and specific snow water content (right column) across the US to solar activity over 6 cases of lag, from zero to five years.

Source: SILSO and ERA5.

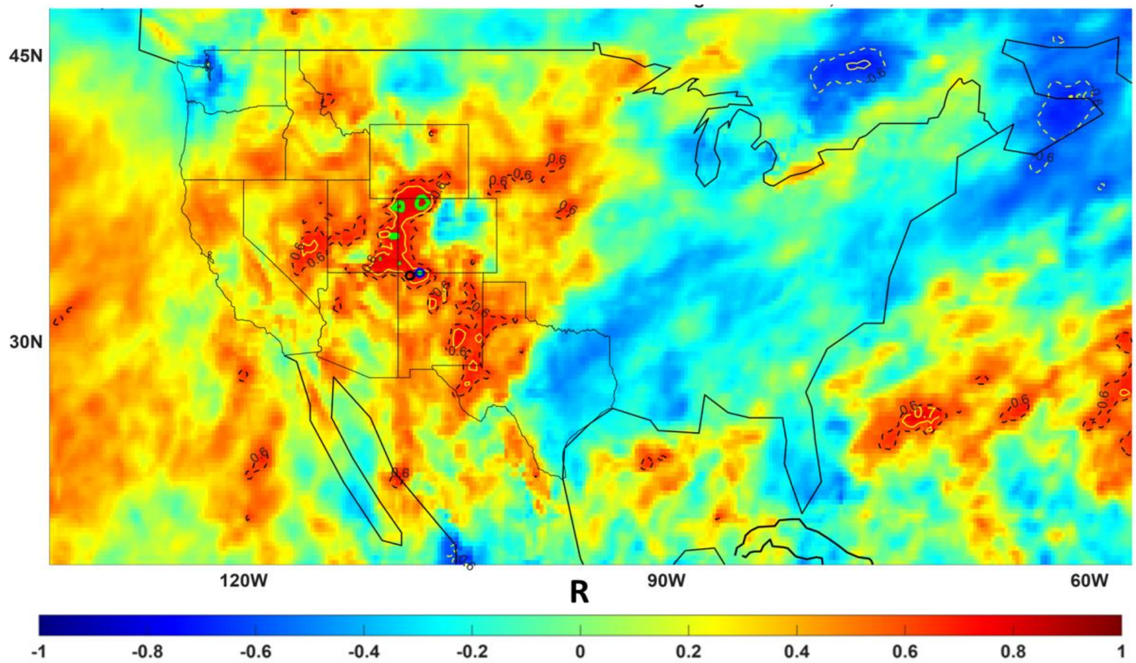

Figure A5. 3 year-lagged correlation of the 5yta SSN series to the 5yta specific rainwater content. Focus over Southwestern US and Southern Rocky Mountains. The open blue circle on the Colorado New Mexico border identifies the location of the 3-year prediction example for specific rainwater content. The adjacent open black circle identifies the location of the Wallace [12] Animas River 3 year prediction example. The four 'X's identify major cities in the area, starting from NE and going clockwise these are Denver, Albuquerque, Phoenix, and Los Angeles.

Source: SILSO and ERA5.

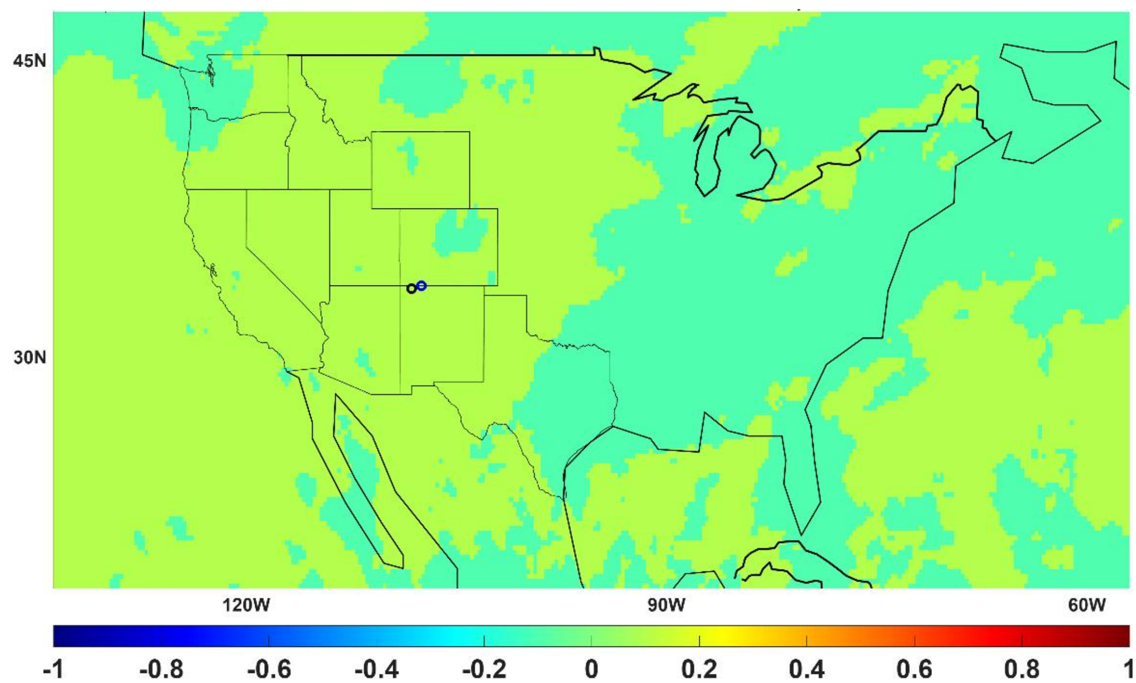

Figure A6. Autocorrelation map of the residual between solar 3 years lagged lagged regression to specific rainwater content (all 5-year trailing averages).

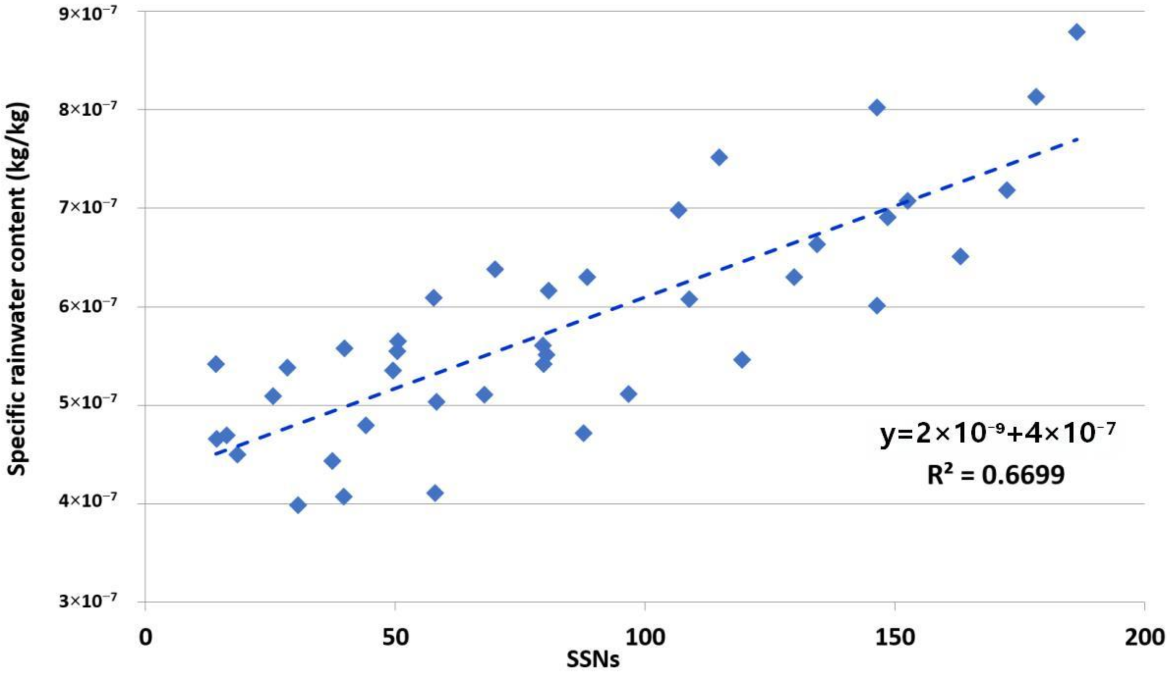

Figure A7. Scatterplot of solar activity (SSNs) vs. specific rainwater content upstream of the USGS Animas River gage near Farmington, New Mexico.

Source: See **Figure 13** and associated text.

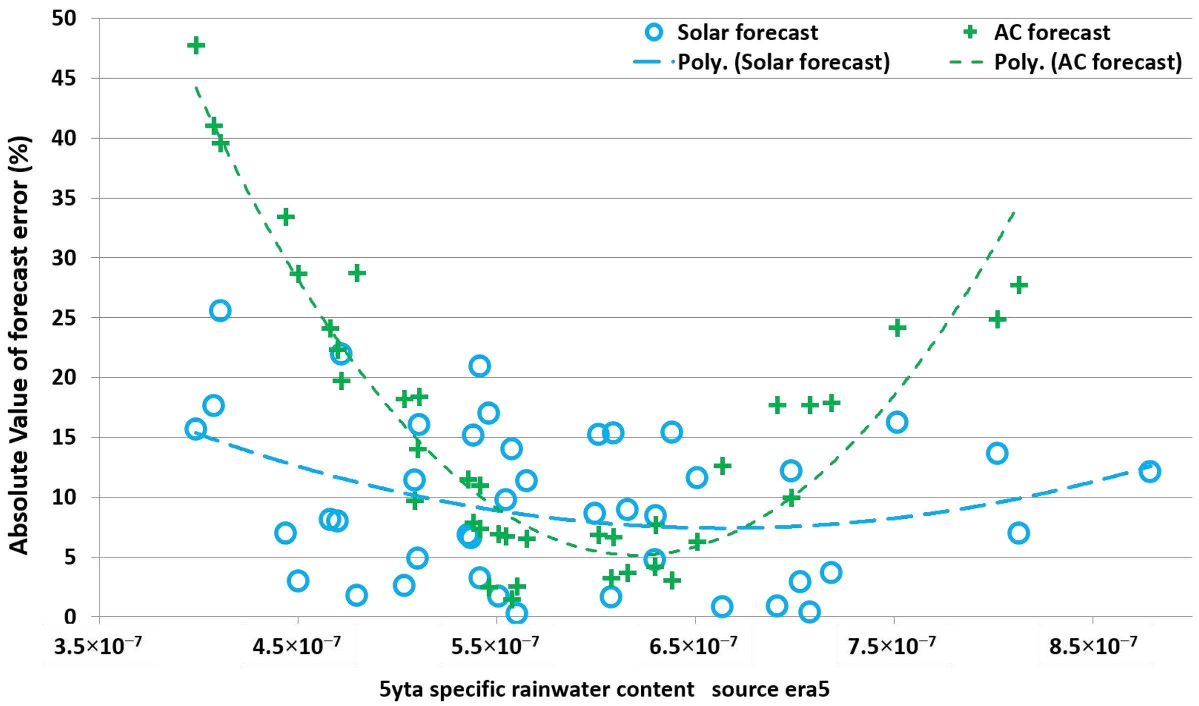

Figure A8. Comparison of Solar to AC hindcast errors for the projection of specific rainwater content upstream of the Animas River site location.

Source: See **Figure 13** and associated text.

```
Model 1: y_stat ~ Lags(y_stat, 1:2) + Lags(x_stat, 1:2)
Model 2: y_stat ~ Lags(y_stat, 1:2)
  Res.Df Df      F    Pr(>F)
1     32
2     34 -2 16.539 1.168e-05 ***
---
Signif. codes:  0 '***' 0.001 '**' 0.01 '*' 0.05 '.' 0.1 ' ' 1
```

Figure A9. Output from Granger run using R for the example projection of specific rainwater content upstream of the Animas River site location.

Source: See **Figure 13** and associated text.

Table A4. Solar hindcast skill via the Nash-Sutcliffe Efficiency metric (NSE) for the example projection of specific rainwater content upstream of the Animas River site location.

Nash Sutcliff Efficiency Metric, NSE			For NSE > 0.5, the Predictive Skill Is Superior to Simple Use of the Average Value		
Size N	**30**	**30**	**Sum Below**	**Sum Below**	**NSE**
Mean	5.80×10^{-7}	5.80×10^{-7}	1.82×10^{-13}	5.30×10^{-13}	0.66
Year	era5 Q4 5yta OBSERVED	Projection _SSN_5yta_3lag_era5_43	$(Obs - Sim)^2$	$(Obs - Mean)^2$	
1983	5.37×10^{-7}	5.72477×10^{-7}	1.26×10^{-15}	1.82×10^{-15}	
1984	5.99×10^{-7}	6.51103×10^{-7}	2.67×10^{-15}	3.93×10^{-16}	
1985	7.03×10^{-7}	7.2328×10^{-7}	4.24×10^{-16}	1.51×10^{-14}	
1986	8.79×10^{-7}	7.72697×10^{-7}	1.13×10^{-14}	8.97×10^{-14}	
1987	8.13×10^{-7}	7.56517×10^{-7}	3.19×10^{-15}	5.45×10^{-14}	
1988	8.02×10^{-7}	6.92837×10^{-7}	1.19×10^{-14}	4.95×10^{-14}	
1989	6.98×10^{-7}	6.13463×10^{-7}	7.20×10^{-15}	1.41×10^{-14}	
1990	6.38×10^{-7}	5.39883×10^{-7}	9.70×10^{-15}	3.45×10^{-15}	
1991	4.80×10^{-7}	4.882×10^{-7}	7.24×10^{-17}	9.98×10^{-15}	
1992	5.65×10^{-7}	5.00963×10^{-7}	4.12×10^{-15}	2.08×10^{-16}	
1993	6.16×10^{-7}	5.61193×10^{-7}	3.01×10^{-15}	1.33×10^{-15}	
1994	7.52×10^{-7}	6.29533×10^{-7}	1.49×10^{-14}	2.96×10^{-14}	
1995	7.08×10^{-7}	7.04963×10^{-7}	7.22×10^{-18}	1.64×10^{-14}	
1996	7.18×10^{-7}	7.4483×10^{-7}	6.99×10^{-16}	1.93×10^{-14}	
1997	6.51×10^{-7}	7.2629×10^{-7}	5.69×10^{-15}	5.08×10^{-15}	
1998	6.30×10^{-7}	6.59743×10^{-7}	9.01×10^{-16}	2.51×10^{-15}	
1999	5.11×10^{-7}	5.93253×10^{-7}	6.74×10^{-15}	4.68×10^{-15}	
2000	5.03×10^{-7}	5.1651×10^{-7}	1.70×10^{-16}	5.80×10^{-15}	
2001	4.44×10^{-7}	4.7473×10^{-7}	9.56×10^{-16}	1.84×10^{-14}	
2002	4.08×10^{-7}	4.7941×10^{-7}	5.16×10^{-15}	2.96×10^{-14}	
2003	4.11×10^{-7}	5.15923×10^{-7}	1.10×10^{-14}	2.84×10^{-14}	
2004	4.72×10^{-7}	5.7538×10^{-7}	1.07×10^{-14}	1.16×10^{-14}	
2005	5.46×10^{-7}	6.38873×10^{-7}	8.62×10^{-15}	1.13×10^{-15}	
2006	6.01×10^{-7}	6.9276×10^{-7}	8.39×10^{-15}	4.65×10^{-16}	
2007	6.91×10^{-7}	6.97153×10^{-7}	3.66×10^{-17}	1.24×10^{-14}	
2008	6.64×10^{-7}	6.68827×10^{-7}	2.83×10^{-17}	7.04×10^{-15}	
2009	6.08×10^{-7}	6.17593×10^{-7}	1.01×10^{-16}	7.82×10^{-16}	
2010	5.42×10^{-7}	5.5933×10^{-7}	3.08×10^{-16}	1.43×10^{-15}	
2011	5.36×10^{-7}	4.9894×10^{-7}	1.35×10^{-15}	1.93×10^{-15}	
2012	3.99×10^{-7}	4.60987×10^{-7}	3.89×10^{-15}	3.28×10^{-14}	
2013	4.50×10^{-7}	4.36753×10^{-7}	1.82×10^{-16}	1.67×10^{-14}	
2014	4.66×10^{-7}	4.28423×10^{-7}	1.42×10^{-15}	1.29×10^{-14}	
2015	5.09×10^{-7}	4.50877×10^{-7}	3.37×10^{-15}	4.99×10^{-15}	
2016	5.58×10^{-7}	4.7958×10^{-7}	6.10×10^{-15}	4.80×10^{-16}	
2017	6.09×10^{-7}	5.15403×10^{-7}	8.72×10^{-15}	8.51×10^{-16}	
2018	5.60×10^{-7}	5.58947×10^{-7}	2.14×10^{-18}	3.69×10^{-16}	
2019	6.30×10^{-7}	5.769×10^{-7}	2.82×10^{-15}	2.54×10^{-15}	
2020	5.51×10^{-7}	5.60527×10^{-7}	8.84×10^{-17}	8.11×10^{-16}	
2021	5.10×10^{-7}	5.35497×10^{-7}	6.27×10^{-16}	4.78×10^{-15}	
2022	5.55×10^{-7}	5.00817×10^{-7}	2.92×10^{-15}	6.14×10^{-16}	
2023	5.38×10^{-7}	4.5681×10^{-7}	6.62×10^{-15}	1.72×10^{-15}	
2024	4.70×10^{-7}	4.32413×10^{-7}	1.40×10^{-15}	1.20×10^{-14}	
2025	5.42×10^{-7}	4.28277×10^{-7}	1.28×10^{-14}	1.45×10^{-15}	

Source: See **Figure 13** and associated text.

Appendix C. Solar Forcing of Climate under a Damped Harmonic Oscillator Model

Ghil et al.'s paper [78] in addition to its many other points of reference, studies a nominally chaotic circulation dynamic process, ie, the so called "double-gyre" problem associated with the divergent streamlines of the NW Pacific and NE Atlantic oceans. Through a quasi-geostrophic (QG) approximation, the exercise explores how the bifurcation of QG winds across those regions into opposing gyres expresses symmetry and asymmetry, based on the time series history of the geospatial mapping.

In alignment, we also interpret the meridional solar correlation dipole as both roughly symmetric and influenced by circulation. The concept of a correlation dipole is abstract, but we anticipate again that high correlation in these cases can serve as proxies for actual parameters such as surface temperature or rainfall. The Ghil et al. paper also explored periodic forcings including anthropogenic forcings and volcanism (p. 16), and they targeted some of the same WG1AR5 climate forcing parameterizations that our study also describes. However, solar activity was not explored. In comparison, our exercises are premised upon the influence of an oscillating solar forcing function with a period of ~11 years, and a damped correlation wave which follows in its wake.

For example, following the peak 2 to 3 year lag in solar correlation, the drop in intensity of correlation with each year of lag, as the perimeter of that correlation expands from each pole, may resemble a forced critically- or over-damped harmonic oscillator. Notably the preceding HC studies such as Held and Hou [76], factored damping into their equations of radiatively-forced meridional transport. We interpret that variations of both the contextual framework and of the damping coefficient itself can be exercised to explore sensitivity of the correlations to that parameter. For example, the progression of the correlation front is not observed so far to oscillate in any of the graphic products developed in this study. Accordingly, damping is essential to fit any of the solar correlation progression data developed here. In this limited scoping perspective, we simply revisit the damping principal within our solar conceptual framework. If solar correlation intensity is defined by ψ, then

$$\psi(t) = A_d e^{-\gamma t} \qquad \text{(A1)}$$

Where γ is a damping coefficient, t is lag time, and A_d is the displacement from the peak correlation. There are many possibilities for the implementation of this framework. Green's function applications come to mind, given their incorporation of a pulse that propagates through a continuum, using the principle of superposition already universally adopted throughout hydrologic applications. For example, the geographical advancement of a flood, following a significant rainfall event is a routinely applied implementation. In many ways this seems to be a suitable metaphor for the dynamic advancement of a solar caused pulse of added energy to the hydrosphere and its subsequent ebbing over time.

References

[1] Gray, L.J., Beer, J., Geller, M., et al., 2010. Solar Influences on Climate. Reviews of Geophysics. 48(4), RG4001. DOI: https://doi.org/10.1029/2009RG000282

[2] Myhre, G., Shindell, D., Bréon, F.M., et al., 2013. Anthropogenic and natural radiative forcing. In: Stocker, T.F., Qin, D., Plattner, G.-K., et al. (eds.). Climate Change 2013: The Physical Science Basis. Contribution of Working Group I to the Fifth Assessment Report of the Intergovernmental Panel on Climate Change. Cambridge University Press: Cambridge, UK. pp. 659–740.

[3] Forster, P., Storelvmo, T., Armour, K., et al., 2021. The Earth's Energy Budget, Climate Feedbacks, and Climate Sensitivity. In Climate Change 2021 – The Physical Science Basis: Working Group I Contribution to the Sixth Assessment Report of the Intergovernmental Panel on Climate Change. Cambridge University Press: Cambridge, UK; New York, NY, USA. pp. 923–1054. DOI: https://doi.org/10.1017/9781009157896.009

[4] Van Dijk, E.J.C., Jungclaus, J., Sigl, M., et al., 2024. High-frequency climate forcing causes prolonged cold periods in the Holocene. Communications Earth & Environment. 5(1), 242. DOI: https://doi.org/10.1038/s43247-024-01380-0

[5] Smith, D.M., Gillett, N.P., Simpson, I.R., et al., 2022. Attribution of multi-annual to decadal changes in the climate system: The Large Ensemble Single Forcing Model Intercomparison Project (LESFMIP). Frontiers in Climate. 4, 955414. DOI: https://doi.org/10.3389/fclim.2022.955414

[6] Otto, F.E.L., 2023. Attribution of Extreme Events to Climate Change. Annual Review of Environment and Resources. 48(1), 813–828. DOI: https://doi.org/10.1146/annurev-environ-112621-083538

[7] Perkins-Kirkpatrick, S.E., Stone, D.A., Mitchell, D.M., et al., 2022. On the attribution of the impacts of extreme weather events to anthropogenic climate change.

Environmental Research Letters. 17(2), 024009. DOI: https://doi.org/10.1088/1748-9326/ac44c8
[8] Risser, M.D., Ombadi, M., Wehner, M.F., 2025. Granger causal inference for climate change attribution. Environmental Research: Climate. 4(2), 022001. DOI: https://doi.org/10.1088/2752-5295/add046
[9] Hammerling, D., Katzfuss, M., Smith, R., 2019. Climate change detection and attribution. In Handbook of Environmental and Ecological Statistics. Chapman and Hall/CRC: London, UK. pp. 789–817.
[10] Didovets, I., Krysanova, V., Nurbatsina, A., et al., 2024. Attribution of current trends in streamflow to climate change for 12 Central Asian catchments. Climatic Change. 177(1), 16. DOI: https://doi.org/10.1007/s10584-023-03673-3
[11] Wang, H., Liu, J., Klaar, M., et al., 2024. Anthropogenic climate change has influenced global river flow seasonality. Science. 383(6686), 1009–1014. DOI: https://doi.org/10.1126/science.adi9501
[12] Wallace, M.G., 2019. Application of lagged correlations between solar cycles and hydrosphere components towards sub-decadal forecasts of streamflows in the Western USA. Hydrological Sciences Journal. 64(2), 137–164. DOI: https://doi.org/10.1080/02626667.2019.1567925
[13] Bracco, A., Brajard, J., Dijkstra, H.A., et al., 2024. Machine learning for the physics of climate. Nature Reviews Physics. 7(1), 6–20. DOI: https://doi.org/10.1038/s42254-024-00776-3
[14] Balaji, V., Couvreux, F., Deshayes, J., et al., 2022. Are general circulation models obsolete? Proceedings of the National Academy of Sciences. 119(47), e2202075119. DOI: https://doi.org/10.1073/pnas.2202075119
[15] Ham, Y.-G., Kim, J.-H., Luo, J.-J., 2019. Deep learning for multi-year ENSO forecasts. Nature. 573(7775), 568–572. DOI: https://doi.org/10.1038/s41586-019-1559-7
[16] Kroll, C.A., Jnglin Wills, R.C., Kornblueh, L., et al., 2025. Parameterization adaption needed to unlock the benefits of increased resolution for the ITCZ in ICON. Atmospheric Chemistry and Physics. 25(22), 16915–16943. DOI: https://doi.org/10.5194/acp-25-16915-2025
[17] Seager, R., Liu, H., Osborn, T.J., et al., 2026. Mediterranean Drying by a Positive North Atlantic Oscillation Trend over the Last 65 Years Is an Extreme Outlier in the CMIP6 Multimodel Ensemble. Journal of Climate. 39(2), 785–804. DOI: https://doi.org/10.1175/JCLI-D-25-0359.1
[18] Stepaniak, D., 2003. Vertically Integrated Mass, Moisture, Heat, and Energy Budget Products Derived from the NCEP/NCAR Reanalysis. Climate Data Guide, NCAR: Boulder, CO, USA.
[19] Nguyen, H., Evans, A., Lucas, C., et al., 2013. The Hadley Circulation in Reanalyses: Climatology, Variability, and Change. Journal of Climate. 26(10), 3357–3376. DOI: https://doi.org/10.1175/JCLI-D-12-00224.1
[20] ECCO Consortium, Fukumori, I., Wang, O., et al., 2021. Synopsis of the ECCO Central Production Global Ocean and Sea-Ice State Estimate, Version 4 Release 4. Zenodo. 1–17. DOI: https://doi.org/10.5281/ZENODO.3765928
[21] Landschützer, P., Bushinsky, S., Gray, A., 2019. A Combined Globally Mapped CO_2 Flux Estimate Based on the Surface Ocean CO_2 Atlas Database (SOCAT) and Southern Ocean Carbon and Climate Observations and Modeling (SOCCOM) Biogeochemistry Floats from 1982 to 2017 (NCEI Accession 0191304). Version 1.1. NOAA National Centers for Environmental Information: Asheville, NC, USA.
[22] Gregory, J.M., Forster, P.M., 2008. Transient climate response estimated from radiative forcing and observed temperature change. Journal of Geophysical Research: Atmospheres. 113(D23), 2008JD010405. DOI: https://doi.org/10.1029/2008JD010405
[23] Paltridge, G.W., 1974. Global Cloud Cover and Earth Surface Temperature. Journal of the Atmospheric Sciences. 31(6), 1571–1576. DOI: https://doi.org/10.1175/1520-0469(1974)031<1571:GCCAES>2.0.CO;2
[24] Beres, J.H., Alexander, M.J., Holton, J.R., 2004. A Method of Specifying the Gravity Wave Spectrum above Convection Based on Latent Heating Properties and Background Wind. Journal of the Atmospheric Sciences. 61(3), 324–337. DOI: https://doi.org/10.1175/1520-0469(2004)061<0324:AMOSTG>2.0.CO;2
[25] Rasch, P.J., Xie, S., Ma, P.-L., et al., 2019. An Overview of the Atmospheric Component of the Energy Exascale Earth System Model. Journal of Advances in Modeling Earth Systems. 11(8), 2377–2411. DOI: https://doi.org/10.1029/2019MS001629
[26] Wang, X., Han, Y., Xue, W., et al., 2022. Stable climate simulations using a realistic general circulation model with neural network parameterizations for atmospheric moist physics and radiation processes. Geoscientific Model Development. 15(9), 3923–3940. DOI: https://doi.org/10.5194/gmd-15-3923-2022
[27] Mantsis, D.F., Lintner, B.R., Broccoli, A.J., et al., 2014. The Response of Large-Scale Circulation to Obliquity-Induced Changes in Meridional Heating Gradients. Journal of Climate. 27(14), 5504–5516. DOI: https://doi.org/10.1175/JCLI-D-13-00526.1
[28] Taylor, K.E., Stouffer, R.J., Meehl, G.A., 2012. An Overview of CMIP5 and the Experiment Design. Bulletin of the American Meteorological Society. 93(4), 485–498. DOI: https://doi.org/10.1175/BAMS-D-11-00094.1
[29] Smith, D.M., Eade, R., Scaife, A.A., et al., 2019. Robust skill of decadal climate predictions. Npj Cli-

mate and Atmospheric Science. 2(1), 13. DOI: https://doi.org/10.1038/s41612-019-0071-y
[30] Labitzke, K., Van Loon, H., 1997. The Signal of the 11-Year Sunspot Cycle in the Upper Troposphere-Lower Stratosphere. Space Science Reviews. 80(3–4), 393–410. DOI: https://doi.org/10.1023/A:1004907126955
[31] Meehl, G.A., Arblaster, J.M., 2009. A Lagged Warm Event–Like Response to Peaks in Solar Forcing in the Pacific Region. Journal of Climate. 22(13), 3647–3660. DOI: https://doi.org/10.1175/2009JCLI2619.1
[32] Xiao, Z., Liao, Y., Li, C., 2016. Possible impact of solar activity on the convection dipole over the tropical pacific ocean. Journal of Atmospheric and Solar-Terrestrial Physics. 140, 94–107. DOI: https://doi.org/10.1016/j.jastp.2016.02.008
[33] Huo, W., Xiao, Z., Zhao, L., 2023. Phase-Locked Impact of the 11-Year Solar Cycle on Tropical Pacific Decadal Variability. Journal of Climate. 36(2), 421–439. DOI: https://doi.org/10.1175/JCLI-D-21-0595.1
[34] Davis, N.A., Birner, T., 2022. Eddy-Mediated Hadley Cell Expansion due to Axisymmetric Angular Momentum Adjustment to Greenhouse Gas Forcings. Journal of the Atmospheric Sciences. 79(1), 141–159. DOI: https://doi.org/10.1175/JAS-D-20-0149.1
[35] Menzel, M.E., Waugh, D.W., Wu, Z., et al., 2024. Replicating the Hadley cell edge and subtropical jet latitude disconnect in idealized atmospheric models. Weather and Climate Dynamics. 5(1), 251–261. DOI: https://doi.org/10.5194/wcd-5-251-2024
[36] Boer, G.J., Sargent, N.E., 1985. Vertically Integrated Budgets of Mass and Energy for the Globe. Journal of the Atmospheric Sciences. 42(15), 1592–1613. DOI: https://doi.org/10.1175/1520-0469(1985)042<1592:VIBOMA>2.0.CO;2
[37] Chavas, D.R., Peters, J., 2023. Static Energy Deserves Greater Emphasis in the Meteorology Community. Bulletin of the American Meteorological Society. 104(10), E1918–E1927. DOI: https://doi.org/10.1175/BAMS-D-22-0013.1
[38] Smyth, T.J., 2011. Penetration of UV irradiance into the global ocean. Journal of Geophysical Research: Oceans. 116(C11), 2011JC007183. DOI: https://doi.org/10.1029/2011JC007183
[39] Kodera, K., 2005. Possible solar modulation of the ENSO cycle. Papers in Meteorology and Geophysics. 55(1/2), 21–32. DOI: https://doi.org/10.2467/mripapers.55.21
[40] Falkowski, P.G., 1994. The role of phytoplankton photosynthesis in global biogeochemical cycles. Photosynthesis Research. 39(3), 235–258. DOI: https://doi.org/10.1007/BF00014586
[41] Barton, P.S., Evans, M.J., Foster, C.N., et al., 2019. Towards Quantifying Carrion Biomass in Ecosystems. Trends in Ecology & Evolution. 34(10), 950–961. DOI: https://doi.org/10.1016/j.tree.2019.06.001
[42] Vreugdenhil, C.A., Gayen, B., 2021. Ocean Convection. Fluids. 6(10), 360. DOI: https://doi.org/10.3390/fluids6100360
[43] Nilsson, J., Körnich, H., 2008. A Conceptual Model of the Surface Salinity Distribution in the Oceanic Hadley Cell. Journal of Climate. 21(24), 6586–6598. DOI: https://doi.org/10.1175/2008JCLI2284.1
[44] Lee, Z., Hu, C., Shang, S., et al., 2013. Penetration of UV-visible solar radiation in the global oceans: Insights from ocean color remote sensing. Journal of Geophysical Research: Oceans. 118(9), 4241–4255. DOI: https://doi.org/10.1002/jgrc.20308
[45] Döös, K., Nilsson, J., Nycander, J., et al., 2012. The World Ocean Thermohaline Circulation. Journal of Physical Oceanography. 42(9), 1445–1460. DOI: https://doi.org/10.1175/JPO-D-11-0163.1
[46] Gayen, B., Griffiths, R.W., 2022. Rotating Horizontal Convection. Annual Review of Fluid Mechanics. 54(1), 105–132. DOI: https://doi.org/10.1146/annurev-fluid-030121-115729
[47] Monismith, S.G., Imberger, J., Morison, M.L., 1990. Convective motions in the sidearm of a small reservoir. Limnology and Oceanography. 35(8), 1676–1702. DOI: https://doi.org/10.4319/lo.1990.35.8.1676
[48] Durden, J.M., Bett, B.J., Jones, D.O.B., et al., 2015. Abyssal hills – hidden source of increased habitat heterogeneity, benthic megafaunal biomass and diversity in the deep sea. Progress in Oceanography. 137, 209–218. DOI: https://doi.org/10.1016/j.pocean.2015.06.006
[49] Kim, J., Son, S., Kim, D., et al., 2020. Discovery of Active Hydrothermal Vent Fields Along the Central Indian Ridge, 8–12°S. Geochemistry, Geophysics, Geosystems. 21(8), e2020GC009058. DOI: https://doi.org/10.1029/2020GC009058
[50] Carroll, D., Menemenlis, D., Adkins, J.F., et al., 2020. The ECCO-Darwin Data-Assimilative Global Ocean Biogeochemistry Model: Estimates of Seasonal to Multidecadal Surface Ocean p CO_2 and Air-Sea CO_2 Flux. Journal of Advances in Modeling Earth Systems. 12(10), e2019MS001888. DOI: https://doi.org/10.1029/2019MS001888
[51] Miyazaki, K., Patra, P.K., Takigawa, M., et al., 2008. Global-scale transport of carbon dioxide in the troposphere. Journal of Geophysical Research: Atmospheres. 113(D15), 2007JD009557. DOI: https://doi.org/10.1029/2007JD009557
[52] Chahine, M.T., Chen, L., Dimotakis, P., et al., 2008. Satellite remote sounding of mid-tropospheric CO_2. Geophysical Research Letters. 35(17), 2008GL035022. DOI: https://doi.org/10.1029/2008GL035022
[53] Bischof, W., Borchers, R., Fabian, P., et al., 1985. Increased concentration and vertical distribution of carbon dioxide in the stratosphere. Nature. 316(6030),

708–710. DOI: https://doi.org/10.1038/316708a0

[54] Andrews, A.E., Boering, K.A., Daube, B.C., et al., 2001. Mean ages of stratospheric air derived from in situ observations of CO_2, CH_4, and N_2O. Journal of Geophysical Research: Atmospheres. 106(D23), 32295–32314. DOI: https://doi.org/10.1029/2001JD000465

[55] Chahine, M., Barnet, C., Olsen, E.T., et al., 2005. On the determination of atmospheric minor gases by the method of vanishing partial derivatives with application to CO_2. Geophysical Research Letters. 32(22), 2005GL024165. DOI: https://doi.org/10.1029/2005GL024165

[56] DeVries, T., 2022. The Ocean Carbon Cycle. Annual Review of Environment and Resources. 47(1), 317–341. DOI: https://doi.org/10.1146/annurev-environ-120920-111307

[57] Wu, Y., Zhao, X., Qi, Z., et al., 2023. Relative Contribution of Atmospheric Forcing, Oceanic Preconditioning and Sea Ice to Deep Convection in the Labrador Sea. Journal of Marine Science and Engineering. 11(4), 869. DOI: https://doi.org/10.3390/jmse11040869

[58] Starr, C., 2015. Ocean Surface CO_2 Flux with Wind Stress. NASA's Scientific Visualization Studio: Greenbelt, MD, USA. Available from: https://svs.gsfc.nasa.gov/4398#section_credits

[59] Brix, H., Menemenlis, D., Hill, C., et al., 2015. Using Green's Functions to initialize and adjust a global, eddying ocean biogeochemistry general circulation model. Ocean Modelling. 95, 1–14. DOI: https://doi.org/10.1016/j.ocemod.2015.07.008

[60] Holton, J.R., Haynes, P.H., McIntyre, M.E., et al., 1995. Stratosphere-troposphere exchange. Reviews of Geophysics. 33(4), 403–439. DOI: https://doi.org/10.1029/95RG02097

[61] Chipperfield, M.P., Bekki, S., 2024. Opinion: Stratospheric ozone – depletion, recovery and new challenges. Atmospheric Chemistry and Physics. 24(4), 2783–2802. DOI: https://doi.org/10.5194/acp-24-2783-2024

[62] Miles, G.M., Siddans, R., Kerridge, B.J., et al., 2015. Tropospheric ozone and ozone profiles retrieved from GOME-2 and their validation. Atmospheric Measurement Techniques. 8(1), 385–398. DOI: https://doi.org/10.5194/amt-8-385-2015

[63] Pound, R.J., Sherwen, T., Helmig, D., et al., 2020. Influences of oceanic ozone deposition on tropospheric photochemistry. Atmospheric Chemistry and Physics. 20(7), 4227–4239. DOI: https://doi.org/10.5194/acp-20-4227-2020

[64] Wang, M., Fu, Q., 2021. Stratosphere-Troposphere Exchange of Air Masses and Ozone Concentrations Based on Reanalyses and Observations. Journal of Geophysical Research: Atmospheres. 126(18), e2021JD035159. DOI: https://doi.org/10.1029/2021JD035159

[65] Dessler, A.E., 2002. The effect of deep, tropical convection on the tropical tropopause layer. Journal of Geophysical Research: Atmospheres. 107(D3). DOI: https://doi.org/10.1029/2001JD000511

[66] Yamamoto, M.K., Oyamatsu, M., Horinouchi, T., et al., 2003. High time resolution determination of the tropical tropopause by the Equatorial Atmosphere Radar. Geophysical Research Letters. 30(21), 2003GL018072. DOI: https://doi.org/10.1029/2003GL018072

[67] Chapman, S., 1930. A theory of upper atmosphere ozone. Memoirs of the Royal Meteorological Society. 3, 103–125.

[68] Anderson, G.P., Clough, S.A., Kneizys, F.X., et al., 1986. AFGL Atmospheric Constituent Profiles (0.120km). No. AFGLTR860110. Air Force Geophysics Laboratory, AFGL: Bedford, MA, USA.

[69] Rosenlof, K.H., Reid, G.C., 2008. Trends in the temperature and water vapor content of the tropical lower stratosphere: Sea surface connection. Journal of Geophysical Research: Atmospheres. 113(D6), 2007JD009109. DOI: https://doi.org/10.1029/2007JD009109

[70] Hsu, J., Prather, M.J., 2009. Stratospheric variability and tropospheric ozone. Journal of Geophysical Research: Atmospheres. 114(D6), 2008JD010942. DOI: https://doi.org/10.1029/2008JD010942

[71] Pollack, I.B., Ryerson, T.B., Trainer, M., et al., 2013. Trends in ozone, its precursors, and related secondary oxidation products in Los Angeles, California: A synthesis of measurements from 1960 to 2010. Journal of Geophysical Research: Atmospheres. 118(11), 5893–5911. DOI: https://doi.org/10.1002/jgrd.50472

[72] Crutzen, P., 1973. A discussion of the chemistry of some minor constituents in the stratosphere and troposphere. Pure and Applied Geophysics. 106–108(1), 1385–1399. DOI: https://doi.org/10.1007/BF00881092

[73] Crutzen, P.J., 1979. The Role of NO and NO_2 in the Chemistry of the Troposphere and Stratosphere. Annual Review of Earth and Planetary Sciences. 7(1), 443–472. DOI: https://doi.org/10.1146/annurev.ea.07.050179.002303

[74] Bien, T., Helmig, D., 2018. Changes in summertime ozone in Colorado during 2000–2015. Elementa: Science of the Anthropocene. 6, 55. DOI: https://doi.org/10.1525/elementa.300

[75] Paltridge, G.W., 1975. Global dynamics and climate - a system of minimum entropy exchange. Quarterly Journal of the Royal Meteorological Society. 101(429), 475–484. DOI: https://doi.org/10.1002/qj.49710142906

[76] Held, I.M., Hou, A.Y., 1980. Nonlinear Axially Symmetric Circulations in a Nearly Inviscid Atmosphere. Journal of the Atmospheric Sciences. 37(3), 515–533. DOI: https://doi.org/10.1175/1520-0469(1980)037<0515:NASCIA>2.0.CO;2

[77] Xian, T., Xia, J., Wei, W., et al., 2021. Is Hadley

Cell Expanding? Atmosphere. 12(12), 1699. DOI: https://doi.org/10.3390/atmos12121699

[78] Ghil, M., Chekroun, M.D., Simonnet, E., 2008. Climate dynamics and fluid mechanics: Natural variability and related uncertainties. Physica D: Nonlinear Phenomena. 237(14–17), 2111–2126. DOI: https://doi.org/10.1016/j.physd.2008.03.036

[79] Rateb, A., R. Scanlon, B., Buzzanga, B., 2026. Structural deficits in large ensembles limit detection and attribution of terrestrial water storage. Communications Earth & Environment. DOI: https://doi.org/10.1038/s43247-026-03772-w

[80] Guemas, V., Auger, L., Doblas-Reyes, F.J., 2014. Hypothesis Testing for Autocorrelated Short Climate Time Series. Journal of Applied Meteorology and Climatology. 53(3), 637–651. DOI: https://doi.org/10.1175/JAMC-D-13-064.1

[81] Trenberth, K.E., 1984. Some Effects of Finite Sample Size and Persistence on Meteorological Statistics. Part I: Autocorrelations. Monthly Weather Review. 112(12), 2359–2368. DOI: https://doi.org/10.1175/1520-0493(1984)112<2359:SEOFSS>2.0.CO;2

[82] Tuel, A., Martius, O., 2023. Weather persistence on sub-seasonal to seasonal timescales: a methodological review. Earth System Dynamics. 14(5), 955–987. DOI: https://doi.org/10.5194/esd-14-955-2023